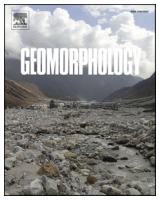
Geomorphology 439 (2023) 108861



Contents lists available at ScienceDirect

Geomorphology

journal homepage: www.journals.elsevier.com/geomorphology





Spatial distribution of rock uplift in the Bongarà district (Peruvian Andes) and implications for the genesis of supergene ore deposits

Anna Sorrentino [a], Ettore Valente [a,*], Nicola Mondillo [a,b]

[a] Department of Earth, Environment and Resources Sciences, University of Naples Federico II, Naples, Italy
[b] Natural History Museum, London, United Kingdom

ARTICLE INFO

Keywords:
River long profile
Chi plot
Ksn index
Differential rock uplift
Ore deposits

ABSTRACT

Topography and river landscape morphometry of two hydrographic basins, the Utcubamba River and the Chiriaco River basins (Bongará district, Amazonas region) allowed to determine the relationship between the irregular distribution of vertical motions (e.g., rock uplift) and the genesis of supergene Zn deposits. The latter derives from variable weathering of pre-existing carbonate-hosted Zn sulfides orebodies, in three distinct localities: Florida Canyon, Mina Grande and Cristal. The research was carried out through the evaluation of the parameters such as elevation, local relief, swath profile, river longitudinal profiles and transformed river profiles (χ-long profiles), and slope/area analysis to derive the normalized channel steepness index (k_{sn}). The NE-ward sharp increase in mean and minimum elevation coupled with a jump in the mean k_{sn} values, suggests that the Chiriaco River basin has experienced more recent rock uplift than the Utcubamba River basin. In fact, the Utcubamba River experienced a long-lasting uplift, resulting in a rugged local relief and lowering the mean and minimum elevations, and exhumation and weathering of the Triassic-hosted sulfide mineral deposits at Florida Canyon. In the Chiriaco River basin, the younger uplift has promoted the weathering of the more surficial Jurassic-hosted Mina Grande and Cristal mineral deposits. The morphometric approach proved to be effective in recognizing fertile areas with near-surface orebodies also in regions characterized by distinct types of ore deposits.

1. Introduction

Supergene ore deposits of metals like Zn, Cu, and Au commonly consist of oxidized minerals deriving from weathering of pre-existing sulfide bodies of hydrothermal origin. Supergene ores represent very interesting targets for mineral exploration because they are surficial, and because they can have higher metal grades and commonly contain less sulfur than former sulfides (e.g. Chavez, 2000; Hitzman et al., 2003). Hydrothermal sulfides can form in many types of geologic environments. Cu-sulfides prevail in the well-known porphyry-Cu systems, which are genetically associated with the emplacement of calcalkaline magmatic intrusions at shallow depths (ca. 2–3 km) on convergent margins (i.e. volcanic arcs) (Sillitoe, 2010). In similar settings, Au is hosted in the so-called "epithermal ores", which are associated with acidic hydrothermal alteration of surficial volcanoclastic rocks (like volcanic domes or ignimbrites), and commonly overlie deeper porphyry Cu deposits (Hedenquist and Arribas, 2022). On the contrary, Zn-sulfide bodies are more typically hosted by sedimentary rocks, either siliciclastic or carbonatic, and form in sedimentary basins on the seafloor or during the diagenesis (Leach et al., 2005). Supergene deposits can form from all these diverse ore types when the sulfide protores are exhumed to near surface environments and interact with groundwaters to be chemically weathered (e.g., Chavez, 2000; Sillitoe, 2005). In this process, a right balance between uplift and erosion at the time of chemical weathering is crucial to form economic supergene ores. Uplift and erosion favour the uncapping of hidden sulfide bodies which have been formed at depth. In addition, tectonic fracturation enhances groundwater circulation promoting chemical weathering of rocks and hosted sulfide minerals. However, under certain climatic conditions characterized by high run-off, a strong uplift can also bring to the complete erosion of the supergene deposits.

The tectonic evolution of an area plays different roles if considering the formation of Cu—Au— or Zn-supergene deposits, because the hypogene protores originally emplace at diverse depths, and at distinct times during the geological evolution of a region. Under favourable climatic conditions, due to their very surficial occurrence, the

* Corresponding author at: Via Vicinale Cupa Cintia 21, 80126 Naples, Italy.
E-mail address: ettore.valente@unina.it (E. Valente).

https://doi.org/10.1016/j.geomorph.2023.108861
Received 9 January 2023; Received in revised form 29 June 2023; Accepted 4 August 2023
Available online 6 August 2023
0169-555X/© 2023 The Authors. Published by Elsevier B.V. This is an open access article under the CC BY license (http://creativecommons.org/licenses/by/4.0/).

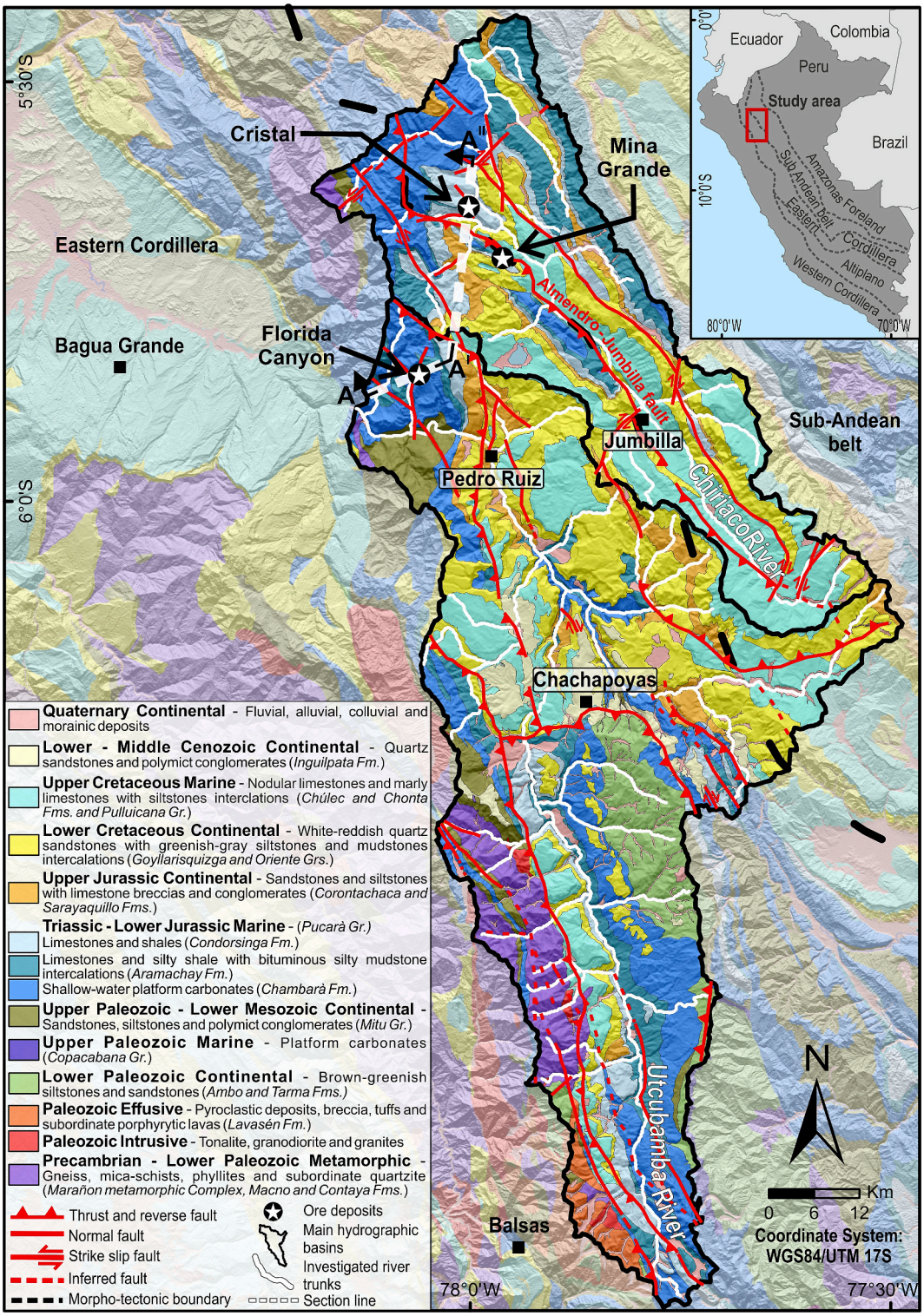


Fig. 1. Simplified geological map of the Utcubamba and Chiriaco River basins plotted on an hillshade map. The map was derived from the geological map of Peru in scale 1:50,000 (https://geocatmin.ingemmet.gob.pe/geocatmin/) grouping the geological units on the basis of their erodibility, depositional setting (continental, marine, volcanic, sub-volcanic and intrusive) and age. The Florida Canyon, Mina Grande and Cristal ore deposits are indicated. The dashed black lines represent the morphotectonic boundaries. The map shows in white the main trunks and their tributaries. White dashed lines A - A″ is the trace of the geological cross section in Fig. 2.

epithermal Au deposits start to be weathered quite early (Boni and Mondillo, 2015; Chavez, 2000; Hitzman et al., 2003; Sillitoe, 2005). If uplift and weathering proceed, epithermal systems are mechanically eroded and deeper porphyry deposits can be ultimately exhumed (Sillitoe, 2010). For example, in the Chilean Andes, where porphyry Cu systems are aligned along tectonic belts of distinct ages, spanning from Late Cretaceous to the Pliocene (Sillitoe and Perelló, 2005), the oldest Eocene-Oligocene Cu-porphyries are characterized by mature supergene alteration blankets, whereas the Pliocene mineralization have been only limited oxidized. The efficiency of the alteration process is strongly

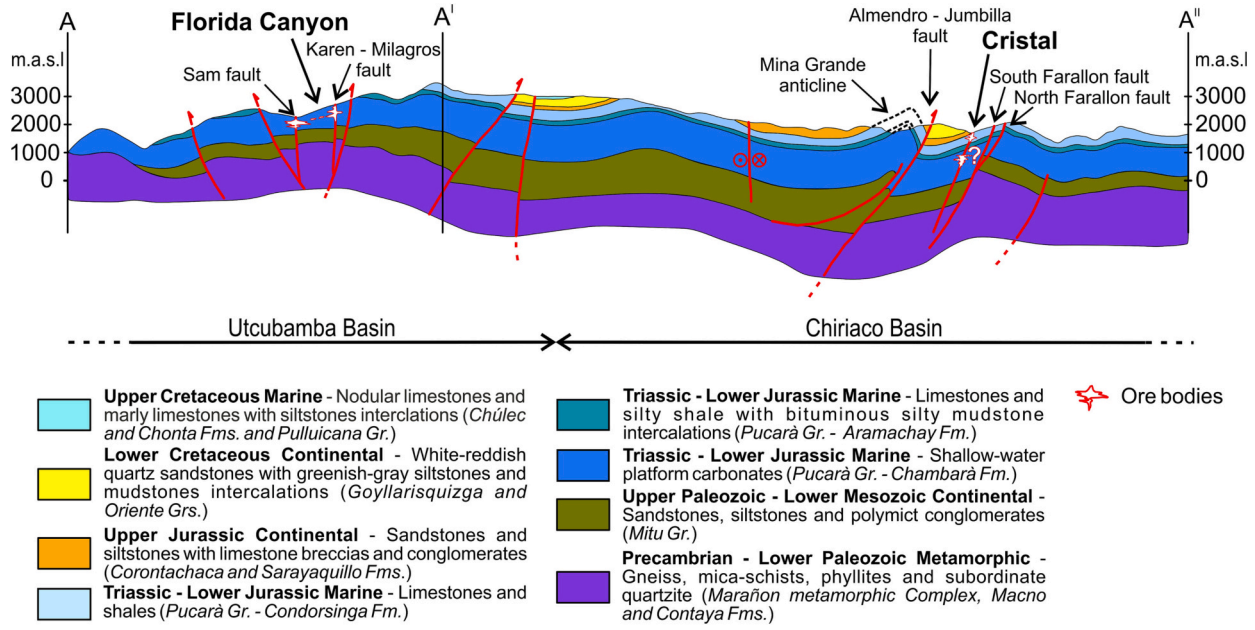


Fig. 2. Geological cross section of the Florida Canyon and Mina Grande-Cristal mineralized areas. (Modified from Anglo Peruana, 2005.)

influenced by the climatic conditions of the area and the nature of the hydrogeologic environment, which can favour the concentration of metals or bring to their leaching and dispersion (Chavez, 2000; Sillitoe, 2005). In the case of the Chilean Cu-porphyries, the Eocene-Oligocene system occurring in the Atacama desert is a paramount example, having been preserved from the mechanical erosion because of the hyper-arid climate which has persisted in the region since 14 Ma (Sillitoe, 2005). Diverse is the case of the sediment-hosted Zn sulfide deposits, which emplace within sedimentary basins and can be exhumed and altered only after basin inversion or well-developed orogenesis (Boni and Mondillo, 2015; Hitzman et al., 2003). Although the mechanism of deposit formation is well known for all the mentioned supergene systems, the relationship between uplift, weathering, and tectonics has been deeply investigated only for understanding the formation of Cu supergene ores (e.g. Sillitoe and McKee, 1996).

The aim of this study is to apply a morphometric approach to better understand the relationship between the distribution of vertical motions (e.g., rock uplift) and the genesis of supergene Zn deposits located in the north-eastern sector of the Peruvian Andean chain. The area of interest is represented by the Bongará district (Amazonas region, northern Peru), which is known as one the best Zn-endowed areas of South America, characterized by several Zn-Pb-sulfide deposits affected by variable degree of weathering. These ores are hosted in Mesozoic carbonate rocks belonging to the Pucará Group (Upper Triassic-Lower Jurassic) (Basuki and Spooner, 2008, 2009; Boni and Mondillo, 2015; de Oliveira et al., 2019a, 2019b, 2021; Reid, 2001). The main mineral deposits of the area are represented by the Cristal and Mina Grande prospects in the north and the Florida Canyon deposit in the south (Arfè et al., 2017b; Basuki and Spooner, 2009; Mondillo et al., 2018a, 2018b; Reid, 2001). Studies conducted by Arfè et al. (2018, 2017b), Chirico et al. (2022), de Oliveira et al. (2019a), suggested that in the Bongará district weathering and alteration of sulfides might have occurred after periods of uplift developed since the late Miocene (e.g. Gregory-Wodzicki, 2000) but an analysis of landscape response to uplift has never been performed.

Considering that the district is located in the Peruvian Andes, straddling across the Eastern Cordillera and the Sub-Andean Fold-and-Thrust belt (SAFTB) (Chacaltana Budiel et al., 2011, 2022; Hunt et al., 2017; Workman and Breede, 2016), and that it is covered by two hydrographic basins (the Utcubamba River and the Chiriaco River), the research has been carried out through the evaluation of parameters such as elevation, local relief, swath profile, river longitudinal profiles, normalized channel steepness index (k_{sn}) and transformed river profiles (χ-long profiles). The spatial distribution of such indexes allowed us to derive important considerations about the spatial distribution of vertical motions and to provide new, general insights on the processes that relate the genesis of supergene deposits to the uplift processes.

2. Study area

2.1. Geological and geomorphological setting

In the northern Andes of Peru three main morphotectonic units are defined (see inset map in Fig. 1): the Western Cordillera, the Eastern Cordillera, and the SAFTB (Carlotto Caillaux et al., 2010; Eude et al., 2015).

The Western Cordillera consists of the Coastal Belt, to the west, in which Jurassic and Cretaceous sedimentary successions are intruded by the Coastal Batholith, and of the Marañon Thrust Belt, to the east, characterized by Mesozoic strata affected by fold and east-verging thrust (Atherton and Webb, 1989; Cobbing, 1985; Pfiffner and Gonzalez, 2013). The Eastern Cordillera is made up of Neoproterozoic-Paleozoic crystalline basement, uplifted along steeply dipping oblique faults, that is overlain by Late Paleozoic and Mesozoic sediments affected by large-scale folding and thrusting (Pfiffner and Gonzalez, 2013). Farther east, the SAFTB consists of east-verging imbricate stack of thrust sheets, related to a thin-skinned tectonics, involving Paleozoic to Cenozoic strata (Mégard, 1984, 1987; Pfiffner and Gonzalez, 2013).

Study area is located at the border between the Eastern Cordillera and the SAFTB where two river basins occur, i.e. the Utcubamba River basin to the west and the Chiriaco River basin to the east. The Utcubamba River basin is entirely straddling in the Eastern Cordillera. The Chiriaco River basin instead lies on the structural border between the Eastern Cordillera and the SAFTB, which matches the Almendro-Jumbilla thrust fault (Figs. 1, 2) (Chacaltana Budiel et al., 2011, 2022). The two rivers run to the NNE (Fig. 3a, b), towards the Amazonas River basin. The landscape in the study area is strongly affected by recent compressive tectonics acting since the Miocene and still active (Chacaltana Budiel et al., 2011, 2022), and is characterized by a

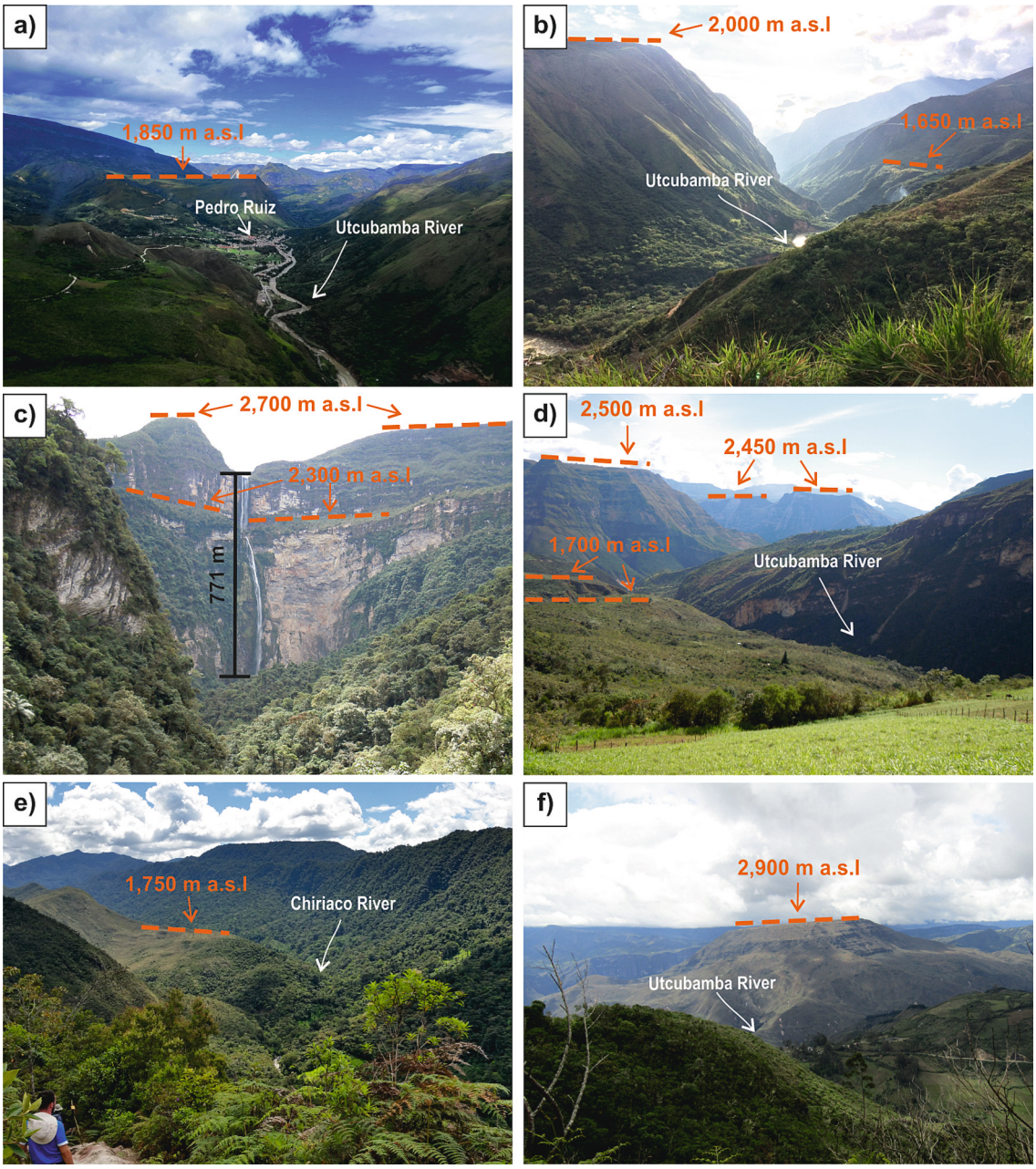


Fig. 3. a) The Utcubamba River and "valley" looking south (it is possible to see the Pedro Ruiz Village; picture taken from Shipasbamba). b) The Utcubamba River looking west (picture taken from Shipasbamba). c) The Gocta waterfall (Cocachimba; river n. 19). d) Utcubamba river valley (picture from river n.19). e) the Cristal River (n. 13), looking north. f) Chachapoyas-Molinopampa area with: hanging low-relief residual surface carved in the continental sandstone of the Goyllarisquizga Group.
(Picture taken from Soloco, looking north.)

combination of steep and abrupt scarp fault-controlled slopes also characterized by waterfalls, including the world-famous Catarata Gocta waterfall that has a total height of 771 m (Fig. 3c), and more gently inclined dip slopes over the Mesozoic rocks (Fig. 3d, e), which outcrop in most of the area covered by the basins. River incisions caused the formation of deep V-shaped valleys and isolated remnants of low-slope surfaces that hang up to some hundred meters above valley bottom (Fig. 3f).

In the Utcubamba R. basin the Precambrian-Lower Paleozoic basement outcrops, forming elongate, NW-SE trending, fault-bounded blocks (Fig. 1) (Chew et al., 2007, 2008). The basement is unconformably covered by up to ~3000-m-thick volcano-sedimentary sequence of the Mitu Group (Lower Triassic) (Fig. 1) (Benavides-Cáceres, 1999; Rosas et al., 2007; Spikings et al., 2016). The latest is uncomfortably overlayed by the Pucará Group, a ~2000 m-thick succession of shallow- to deep-water marine carbonates of Upper Triassic to Lower-Middle Jurassic age (Fig. 1) (Fontbote and Gorzawski, 1990; Reid, 2001; Rosas et al., 2007). The Pucará Group is stratigraphically subdivided into the basal Chambará Formation (Upper Triassic), the intermediate Aramachay Formation (Lower Jurassic) and the uppermost Condorsinga Formation (Lower-Middle Jurassic). The Chambará Formation consists of shallow-water platform carbonates, and has an approximate thickness between 650 m and 750 m (Basuki et al., 2008; Hunt et al., 2017; Reid, 2001; Rosas et al., 2007; Sánchez Fernández, 1995). Stratigraphically above the Condorsinga Formation, the Corontachaca and Sarayaquillo Formations (Middle-Upper Jurassic) lie in angular unconformity (Fig. 1).

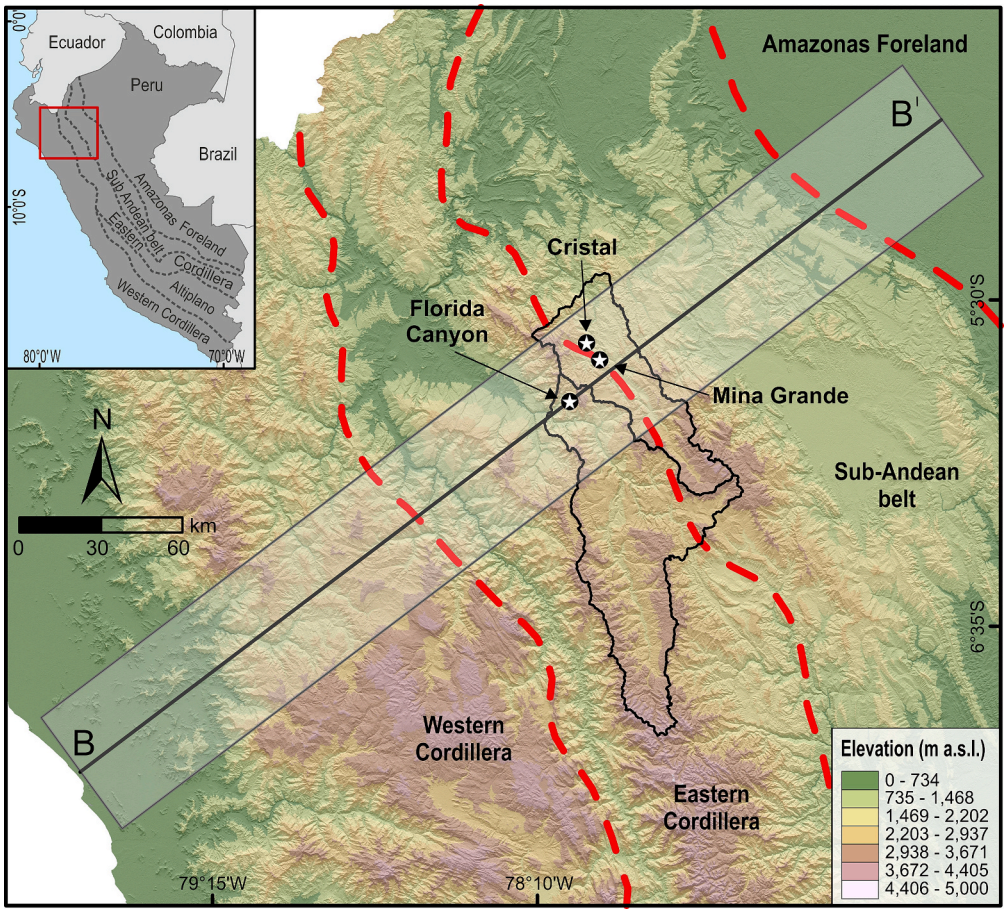


Fig. 4. Elevation map of the northern sector of the Peruvian Andes on which are plotted, with white stars and black circles, the positions of the three main mineral deposits of the Bongará district. The dashed red lines depict the boundaries between the morphotectonic domains derived from Carlotto Caillaux et al. (2010). The black trace BB′ is the centre of the 50-km-wide and 400-km-long swath profile shown in Fig. 5. Black lines indicate location of the investigated hydrographic basins. (For interpretation of the references to colour in this figure legend, the reader is referred to the web version of this article.)

The Corontachaca Formation outcrops mainly in the northern part of the Utcubamba River basin and consists of coarse limestone boulder breccias and breccia-conglomerates. The Sarayaquillo Formation is composed of a 200 m-thick colluvial, alluvial and lacustrine sequence of red-bed, intercalated mudstones, and siltstones with minor conglomeratic horizons and gypsum beds. The continental siliciclastic rocks of the Goyllarisquizga and Oriente Groups (Early Cretaceous) (Fig. 1), respectively in the Utcubamba and Chiriaco River basins, lay unconformably over the Sarayaquillo Formation. The Mesozoic sequence is closed by marine shales, marls and limestones of the Chonta-Chulec Formation (Lower – Upper Cretaceous) (Fig. 1). The younger Cenozoic rocks consist mainly of conglomerates, sandstone and mudstone deposited in fluvial, alluvial and colluvial environments during the Andean uplift phases (Brophy, 2012; Mathalone, 1995; Reid, 2001; Sánchez Fernández, 1995).

Tectonic evolution started in the Late Cretaceous with the Peruvian phase which affected the Paleozoic rocks of the eastern side of the Western Cordillera (Mégard, 1978). During the Paleocene-Eocene, due to the Incaic phases I and II, the deformation propagated eastward forming the Marañon Thrust Belt. Lately, the Miocene-Pliocene Quechua compressional phases (Quechua I at ca. 19 Ma, Quechua II at ca. 10 Ma, and Quechua III at ca. 5 M) promoted the deformation of the Eastern Cordillera and the SAFTB (Mégard, 1984, 1987; Pfiffner and Gonzalez, 2013). Since the late Miocene, deformation has been focused in the Subandean zone (Eude et al., 2015).

Most of studies on the uplift in the Andean chain are focused on the Central Andes and recognize that uplift of the Altiplano has occurred since 40 Ma (Allmendinger et al., 1997; Capitanio et al., 2011; Isacks, 1988; Sempere et al., 1990). A few fission tracks investigations allowed to determine two cooling events in the Eastern Cordillera and central Andes, at 22 Ma and at 10–15 Ma respectively (Benjamin et al., 1987; Laubacher and Naeser, 1994). Relatively recent works support a period of very rapid uplift between 10 and 4 Ma (e.g. Garver et al., 2005; Garzione et al., 2008; Gregory-Wodzicki, 2000).

Three erosional surfaces are recognized at the scale of the chain in response to uplift since the middle Miocene: the Puna, Vallé, and Cañon (Cobbing et al., 1981, 1996; Myers, 1980). The oldest Puna surface is widely recognized in the Andes (Bowman, 1906; Coltorti and Ollier, 1999; Tosdal et al., 1984), and is characterized by a nearly flat surface, now at 4200–4400 m (Wilson et al., 1967). The Vallé surface was cut in response to the initial surface uplift of the Andes in northern Peru in the Middle to Late Miocene. The most recent Cañon stage was characterized by 2000–3000 m canyon incision into the Puna and the Vallé surfaces in response to base level fall and/or surface uplift since Pliocene to Recent (Garver et al., 2005, and references therein; Myers, 1976).

In northern Peruvian Andes, uplift data have been derived by thermochronological analysis conducted along transects across the orogen located a few hundred kilometres south with respect to our study area (e.g., Eude et al., 2015; Michalak et al., 2016). To correlate the timing of deformation and exhumation of thrust structures, Eude et al. (2015) considered a 500 km-long SW-NE profile across the Eastern Cordillera, the SAFTB and the Maranon basin, passing <50 km south of Balsas and Tarapoto. The study comprised the construction of a large-scale balanced cross section, apatite fission track (AFT) analyses, (U—Th)/He (AHe) dating, and vitrinite reflectance (Ro) measurements. Samples were taken from the Paleozoic granitoids of the Eastern Cordillera, and the Late Jurassic and Oligocene sedimentary rocks of the SAFTB. From these investigations, it was argued that thrust systems of the SAFBT and eastern foreland basin were driven by the reactivation of pre-existing Paleozoic thrust and normal faults, suggesting also that rock exhumation was produced by erosion in response to thrust-related uplift (Eude et al., 2015). The authors proposed that at the end of Early Cretaceous

the reference level was the sea level, because the Aptian-Albian Formations are composed of marine to continental deposits. An early Miocene stage (ca. 17 Ma) was constrained by AFT cooling ages in both the Eastern Cordillera and the SAFTB, assuming at this stage a topographic slope similar to today. The authors estimated a minimum horizontal shortening in the Eastern Cordillera of 45 km, on a total shortening of 49 km. Through the AHe cooling ages, the authors constrained a late Miocene stage (~8 Ma), and estimated that 69 km of shortening were accommodated by SAFTB thrusts between ca. 17 and 8 Ma. From these investigations, it was then derived that the propagation of the thrust wedge started between 30 and 24 Ma in the east of the Eastern Cordillera, and between 24 and 17 Ma in the SAFTB (Eude et al., 2015). The authors also calculated that 29 km of shortening occurred during the last 8 Ma. Eude et al. (2015) could not obtain ages older than 17 Ma and calculated the onset of compressional deformation at 24–30 Ma on the basis of the average shortening rates. In any case, all the ages obtained by Eude et al. (2015) agreed with the presence in the Oligocene of a foredeep depozone in the place of the present Easter Cordillera and SAFTB, with maximum thickness of 6.2 ± 0.3 km. At this time, ongoing deformation in the Western Cordillera was driven by basin inversion (e.g. Mégard, 1984).

Following the work of Eude et al. (2015), Michalak et al. (2016) used low-temperature (U—Th)/He thermochronology of zircon and apatite from late Paleozoic granitoids located in the Balsas region, with the aim to better constrain the exhumation history of the Eastern Cordillera. The results of these investigations showed that the samples were characterized by ZHe ages spreading from Paleozoic to Mesozoic, whereas the AHe ages were limited at mid-late Miocene (10.7 ± 1.8 Ma to 8.1 ± 1.2 Ma). These data were interpreted suggesting the occurrence of a slow cooling throughout the Mesozoic and of an accelerated cooling since the mid–late Miocene to the Present. Using a geothermal gradient of 30 °C/km and a temperature of maximum burial depth of ~180 °C, Michalak et al. (2016) calculated a crustal thickness between the ZHe and AHe closure isotherms of 4 km, and thus, a maximum time-averaged exhumation rate from the Late Cretaceous (the time of maximum burial) to the mid–late Miocene (onset of rapid cooling) of ~0.08 mm/yr or less. The mid–late Miocene cooling was estimated to start between 14 and 10 Ma, being considered broadly synchronous at the regional scale and related to rock exhumation, and was accompanied by river incision and uplift. In fact, Michalak et al. (2016) correlated this phase of rock exhumation with the incision and abandonment of the paleosurfaces described in the Western Cordillera and western flank of the northern Peruvian Andes.

Michalak et al. (2016) argued that the timing of initiation of incision and the increased erosion was related to a regional shift to a more humid climate. This hypothesis was however already ruled out by Eude et al. (2015), who had instead invoked the occurrence of thick-skinned thrusts underlying thin-skinned structures to produce steepening of the topography and increasing of the erosion rates.

The above described tectonic evolution has a strong influence on the distribution of elevation. In fact, highest elevations (marked by dark brown colours in Fig. 4) are clustered in the Western and Eastern Cordilleras with values also exceeding ~3500–4000 m a.s.l. These high elevation areas are roughly NW-SE oriented and correspond with areas where rock-types with high resistance to erosion crop out (e.g., the carbonate sequences and the crystalline rocks of the basement). Moving to the NE (i.e., towards the SAFTB) elevation tends to decrease even if an area with values around 3500 m a.s.l. occurs at the boundary between the Eastern Cordillera and the SAFTB (e.g., near Mina Grande and Crystal mining areas). The lowest elevations, depicted by greenish colours in Fig. 4, occur in correspondence of the Pacific coast and the Amazonas Foreland where Cenozoic continental deposits are exposed.

2.2. Ore deposits and climate

The main ore deposits of the Bongará district, Cristal Mina Grande and Florida Canyon, are hosted in the carbonate rocks of the Pucará Group. The Florida Canyon deposit occurs in the Utcubamba River basin running across the Eastern Cordillera. The Zn—Pb mineralization outcrops locally at elevations ranging from 2000 m a.s.l. to approximately 2400 m a.s.l., and comprises both Zn—Pb sulfides and supergene oxidized ores (i.e. the Sam and Karen-Milagros faults; Fig. 2) (Hunt et al., 2017). The deposit is hosted in the lower Chambará Formation as stratabound horizons and breccia type ores in a broad anticlinal structure, bounded by faults (Basuki et al., 2008; Chirico et al., 2022; de Oliveira et al., 2019a, 2019b). The Zn supergene oxidized mineralization represents one third of the total resource in the Florida Canyon area and consists of smithsonite and hemimorphite, and, less commonly, cerussite and hydrozincite (Chirico et al., 2022; de Oliveira et al., 2019a). Studies conducted by Basuki and Spooner (2009) and de Oliveira et al. (2020) argue that the sulfide emplacement occurred after burial and tectonics during the Late Cretaceous (~86–83 Ma), at ~2000–3000 m depth in the sedimentary basin. The secondary supergene ores formed at the expense of primary sulfide ore bodies via multistage supergene processes under tropical-humid climate, which affected the Bongará area since the Miocene, when the sulfides were exhumed (Chirico et al., 2022).

The Cristal and Mina Grande deposits are located at the boundary between the Eastern Cordillera and the SAFTB, in the Chiriaco River basin. Both the mineralization consist mainly of supergene oxidized ores mixed with minor amounts of residual sulfides, and are hosted in carbonate rocks of the Condorsinga Formation (Brophy, 2012). The Mina Grande deposit outcrops on the crest of a tight and overturned NE-verging ramp anticline, in the hanging wall of the Almendro - Jumbilla thrust fault, at altitudes ranging between 1920 and 2260 m a.s.l. (Chacaltana Budiel et al., 2022; Peruana, 2005). The mineralized body covers an area 1500 m long by 400 m wide and extends from the surface up to depths of 20 to 60 m (Arfè et al., 2017b; Peruana, 2005; Wright, 2010). The mineralization consists almost entirely of oxidized minerals, primarily hydrozincite with lesser amounts of smithsonite and hemimorphite, occurring as replacements or concretionary cements in various generations of collapse breccia in karst cavities of Tertiary age, developed and deepened along northwest-southeast fractures and locally along stratification joints (Arfè et al., 2017a, 2017b). The Cristal prospect is located in a faulted block, confined by the Almendro - Jumbilla thrust fault and by the South Farallon fault (Brophy, 2012; Peruana, 2005). The mineralization crops out at elevations between 1600 and 2000 m a.s.l. over an area of about 2 km^2 (Fig. 2) and consists of both sulfide and oxidized bodies (Arfè et al., 2018; Brophy, 2012; Mondillo et al., 2018a). Although both the Cristal and Mina Grande ores are located in a higher stratigraphic position within the Pucará Group than the Florida Canyon one, the primary sulfides formation occurred at the same time in both mining areas (i.e., in the Cretaceous; Arfè et al., 2017b; Mondillo et al., 2018a). The supergene phases are considered to have derived from the oxidation of the exhumed pre-existing sulfides since the Late Miocene (Arfè et al., 2018).

Several authors agree that climatic conditions in the north-eastern domains of the Amazonian South American Andes (e.g., Northern Peru, Ecuador, and Colombia) were being similar to the present-day climate during the last ~20 Ma (e.g., Hoorn et al., 2010). Therefore, since the Miocene, surficial weathering developed in the study area under tropical climate regime, characterized by average annual temperatures between 23°–25 °C, and average annual rainfall exceeding 1000 mm/y (Arfè et al., 2018, and references therein; Chacaltana Budiel et al., 2022).

3. Methodology

3.1. Materials

The morphometric analysis was conducted with the aim of unravelling the spatial distribution of vertical motions, e.g. rock uplift. The

analysis has been carried out through ArcGIS 10.8 © and MATLAB © software. Elevation data were obtained using the shuttle radar topography mission (SRTM) Digital Elevation Model of 3 arc-second (~90 m) in resolution, and freely available at https://earthdata.nasa.gov/ (last access on 18 May 2022). The DEM mosaic was pre-processed by filling sinks through interpolation techniques to obtain a homogenous dataset without data-void pixels.

To highlight the role of rock erodibility on the spatial distribution of morphometric indices a simplified geological map (Fig. 1) of the study area was derived from a regional scale geological map (in scale 1:50,000), available as a shapefile format at https://geocatmin.ingemmet.gob.pe/geocatmin/. Erodibility, depositional setting and age are the criteria adopted for grouping the geological units. Furthermore, faults of regional importance were also reported on the map to verify a possible tectonic control on morphotectonic indexes.

3.2. Topography features

Topography features have been analysed through the construction of two SW-NE trending swath profiles, which pass through the three mineralized deposits. The SwathProfiler Add-In of ArcMap (Pérez-Peña et al., 2017) was used to derive the swath profiles from the 90 m Nasa SRTM DEM. One swath profile crosses the northern sector of the Andean chain, from the Western Cordillera to the Amazonas Foreland, along a 400 km long and 50 km wide transect. The second one is restricted to the study area and crosses the Eastern Cordillera and the SAFTB, along a 48 km long and 10 km wide transect. The transects were chosen to be as more perpendicular as possible to the major morphotectonic features. The maximum, mean and minimum elevation curves were then derived. Maximum elevation mainly depends on the resistance to erosion of the outcropping rocks, mean elevation is considered to be representative of uplift distribution, and minimum elevation represents the elevation of the valley floors and so it is the ideal surface of the local base level (England and Molnar, 1990; Valente et al., 2019). The local relief is also considered a robust indicator of uplift (Basilici et al., 2020; DiBiase et al., 2010; Telbisz et al., 2013) and was determined as the difference between maximum and minimum elevation curves within the swath profiles.

3.3. River network features

The river network features were analysed for the Utcubamba River and the Chiriaco River drainage basins by the construction of the rivers longitudinal profiles (Hack, 1957), the transformed river long profile or chi plots (Perron and Royden, 2013), and the slope-area analysis to extract information about the spatial distribution of the normalized channel steepness index (k_{sn}) (Snyder et al., 2000). Investigated rivers include 14 tributaries of the Chiriaco River basin and 27 tributaries of the Utcubamba River basin. Firstly, we analysed the longitudinal profiles of the selected bedrock rivers. Deviations from the theoretical graded, concave upward profile (Hack, 1957) characterize rivers in a transient state of adjustment to a base-level, tectonics, climatic or rock-type perturbation (Molin et al., 2004). Convex segments are called knickpoints or knickzones, depending upon their length compared to the total stream length, and mark the location of transient signals (Olivetti et al., 2012; Robustelli, 2019; Schoenbohm et al., 2004).

The 41 selected trunks were also investigated following the slope/area analysis by means of the Matlab tool TopoToolbox (Schwanghart and Kuhn, 2010; Schwanghart and Scherler, 2014). This analysis suggest that the slope of bedrock river is inversely proportional to the drainage area (Flint, 1974; Hack, 1957; Kirby and Whipple, 2001; Snyder et al., 2000; Whipple and Tucker, 1999), following the equation:

$$S = k_s A^{-\theta} \tag{1}$$

where S is the slope at the reach scale, A is the drainage area, k_s and θ are the steepness and concavity indexes, respectively. The concavity index (θ) is obtained by the ratio between two positive constants, m and n, that depend on basin hydrology, channel geometry, and erosion processes (Howard et al., 1994; Whipple et al., 2000; Whipple and Tucker, 1999):

$$\theta = \frac{m}{n} \tag{2}$$

The steepness index (k_s) is a function of the uplift rate (U) and an erosion coefficient (K):

$$k_s = \left(\frac{U}{K}\right)^{\frac{1}{n}} \tag{3}$$

The channel steepness index provides a measure of the relative uplift rate and can be used to explore and infer spatial variations in rock uplift (DiBiase et al., 2010; Kirby and Whipple, 2001; Snyder et al., 2000; Van Laningham et al., 2006). When comparing rivers with different length and drainage area, a reference value of the concavity index, θ_{ref}, must be defined because small variations and uncertainties in θ can greatly influence the value of k_s (Kirby and Whipple, 2012). In our analysis, a θ_{ref} value of 0.37 was calculated by averaging the best fit m/n value for each of the 41 investigated rivers, thus allowing us to derive the normalized steepness index (k_{sn}). The k_{sn} index is considered to be an indicator of active uplift, besides enhanced river incision and bedrock erodibility (DiBiase et al., 2010). The spatial distribution of the k_{sn} index is shown both in map view and in a curve showing the average k_{sn} values centred within the swath profile that crosses the mining districts. To derive this curve, k_{sn} values were converted from a vector format to a raster format through an interpolation method to derive the k_{sn} map. We then applied the swath profile method to the k_{sn} map and derived the spatial distribution of the mean k_{sn} values.

The 41 investigated rivers were also investigated by transforming river long profile into chi plots. This approach reduces the noise related to topographic data and allows a clearer identification of transient signals (Perron and Royden, 2013). In the chi plot, the distance horizontal coordinate is transformed to an integral quantity with units of length, called χ (Perron and Royden, 2013). The χ quantity is obtained by integrating inverse of drainage area with respect to distance from base level (x_b) (Gallen and Wegmann, 2017; Perron and Royden, 2013):

$$\chi = \int_{x_b}^{x} \left(\frac{A_0}{A(x)}\right)^{\frac{m}{n}} dx \tag{4}$$

Bedrock rivers dissecting a uniform substratum and equilibrated with uplift are characterized by a linear chi plot, whose slope reflects the uplift rates. Variations from this shape may be due either to variable erodibility or temporally or spatially variable uplift that manifested in the formation of knickpoints in correspondence of break in slope between two linear segments (Perron and Royden, 2013). To derive the chi plot, we used the ChiProfiler function of Matlab (Gallen and Wegmann, 2017), and we adopted a smoothing window of 250 m and a reference drainage area of 1 km^2. To derive the chi plot it is crucial to derive the best fit m/n at the basin scale, and we derived this value for each of the investigated river by the mnotpim script of TopoToolbox (Schwanghart and Kuhn, 2010; Schwanghart and Scherler, 2014). To compare rivers of different length and drainage areas, it is common to use the average m/n value between all the investigated rivers. In our analysis, we derived an average value of 0.37 (θ_{ref}). Noteworthy, to verify a possible lithologic control on the genesis of knickpoints, we adopted the method described in Buscher et al. (2017): knickpoints that are placed within 200 m from lithological contacts have been classified as "lithology controlled knickpoints", whereas knickpoints that are >200 m far from lithological contacts have been classified as "non-lithology controlled knickpoints. To highlight the role of lithology we also added a colour bar on top of both the river long profiles and the chi plots, which is representative of the rock-types mapped in Fig. 1.

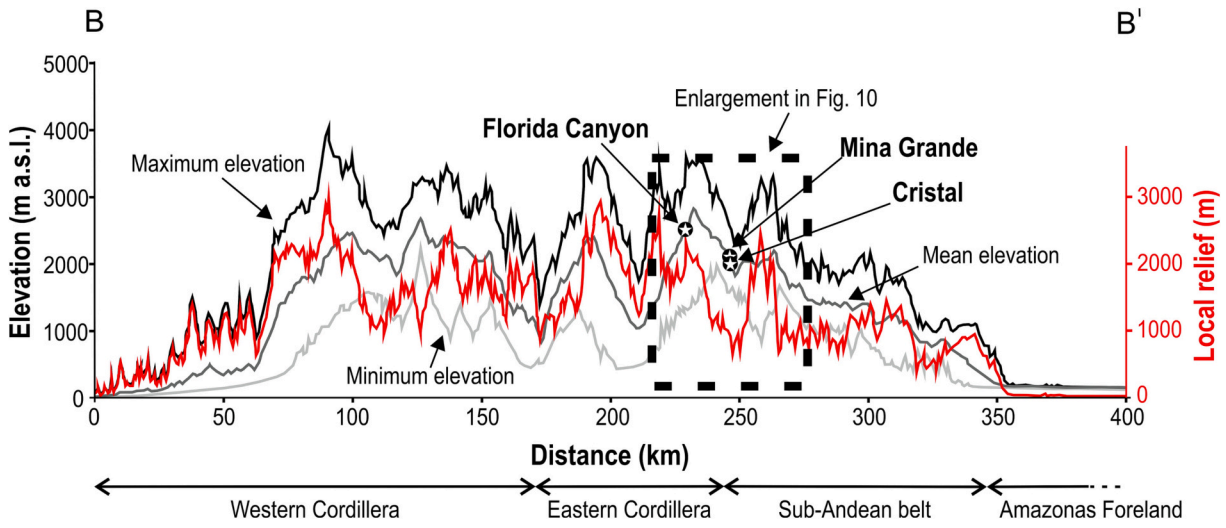


Fig. 5. The swath profiles show the maximum, mean and minimum elevations and local relief. It is centred along the trace of the section BB′ (see Fig. 4 for location) and crosses all the morphotectonic domains and the mineral deposits. Dashed black box shows the location of Fig. 11.

4. Results

4.1. Large-scale topography features

Regional scale features of topography are synthesized in the SW-NE-oriented swath profile of Fig. 5.

The profile passes through the Western Cordillera in the first 155 km and is characterized by low elevations in the Pacific coast that gradually increase towards the NE. A steep escarpment at ~55 km marks the beginning of a dome-like broad area with high maximum, mean and minimum elevation, which extend up to 160 km until the boundary between the Western Cordillera and the Eastern Cordillera. The local relief in this area is rugged because of diffuse river incision. From 160 km to 245 km, across the Eastern Cordillera, the maximum elevation curve exhibits two peaks around 200 km and 230 km that are mirrored by the mean elevation curve. Noteworthy, the peak in the mean elevation at 230 km occurs near Florida Canyon and it is the highest along the entire swath profile (i.e., mean elevation around 3000 m). Minimum elevation curve also exhibits two peaks, which do not correspond with peaks in the maximum and mean elevation. Moreover, a minimum elevation peak around 2000 m a.s.l. occurs near Mina Grande and Cristal mining areas at 240 km and is the culmination of a large area with high values that extends from 235 km to 255 km (at the border of the Eastern Cordillera and the SAFTB). Local relief in the Eastern Cordillera decreases towards the NE, with a local minimum of 1000 m in correspondence with the high minimum elevation area centred near Cristal mining area. Swath profile then moves in the SAFTB from 245 km to 345 km. Elevation curves decrease towards the NE with the highest peak in the maximum elevation curve of 3500 m a.s.l. that occurs at 260 km. Mean elevation exhibits a large high value area (with mean elevation around 2000 m) between 250 km and 270 km, then it continuously decreases towards the NE. The minimum elevation exhibits the above-mentioned maximum at a distance of 255 km at the boundary between the Eastern Cordillera and the SAFTB, and then decreases towards the NE, with a local maximum around 1500 m at a distance of 270 km. Local relief in the SAFTB exhibits a maximum around 2000 m at a distance of 260 km (i.e., in the surroundings of the Mina Grande area) that sharply decreases to a large area with values around 1000 m that extends from 265 km to 320 km. Another jump in the local relief at 320 km marks its sharp decrease in the Amazonas Foreland, a trend that is locally interrupted by a peak around 1000 m at a distance of 345 km. In the last 40 km, the swath profile is characterized by an abrupt reduction

Table 1
Synthesis of the topography features in the different morphotectonic setting depicted by the swath profile in Fig. 4.

	Western Cordillera	Eastern Cordillera	Sub-Andean Fold and Thrust Belt	Amazonas
Maximum elevation	~1000–1500 m in the first 55 km, then a sharp jump up to 4000 m around 90 km. It then stabilizes around 3000–3500 m up to 155 km and it decreases up to 1500 m at the boundary with the Eastern Cordillera. First order wavelength ~50 km	Three peaks at 3500 m around 200, 220 and 230 km, minimum value around 2000 m at 210 km. First order wavelength ~40 km	Highest peak ~3500 m at 260 km then it constantly decreases up to its minimum ~500 m at 345 km at the boundary with the Amazonas foreland. First order wavelength ~20 km	Values ~200 m
Mean elevation	~200–300 m in the first 55 km, then a sharp jump up to 2500 m at 130 km with a slight decrease up to a minimum of 1000 m at the boundary with the Eastern Cordillera. First order wavelength ~50 km	Two peaks at 2500 m around 200 km and 230 km, minimum value around 1200 m at 210 km. First order wavelength ~40 km	Highest peak ~3000 m at 260 km then it constantly decreases up to its minimum ~200 m at 345 km at the boundary with the Amazonas foreland. First order wavelength ~20 km	Values ~200 m
Minimum elevation	~100–200 m in the first 70 km, then it slightly increases up to 2200 m at 130 km, and it decreases up to a minimum of 500 m at the boundary with the Eastern Cordillera. First order wavelength ~25 km	Highest peak ~2000 m at 240 km at the boundary with the SAFTB. Minimum value ~500 m at 210 km. First order wavelength ~40 km	Highest peak ~1500 m at 255 km then it constantly decreases up to its minimum ~100 m at 345 km at the boundary with the Amazonas foreland. First order wavelength ~20 km	Values ~200 m
Local relief	~ 500 m in the first 25 km, then it increases up to 1500 m from 25 km to 55 km. Then a sharp jump up to its maximum ~3000 m at 90 km and it looks rugged up to 155 km with a maximum ~2000 m. First order wavelength ~25 km	Two peaks ~3000 m around 200 km and 220 km, which is interrupted by a local minimum value around 1300 m at 210 km. The lowest value is ~1000 m at 240 km. First order wavelength ~30 km	Highest peak ~2000 m at 260 km, then it decreases ~1000 m from 265 km to 320 km. From 320 km to 345 km values are ~500 with a local maximum ~1000 m at 335 km. First order wavelength ~20 km	Values close to 0 m

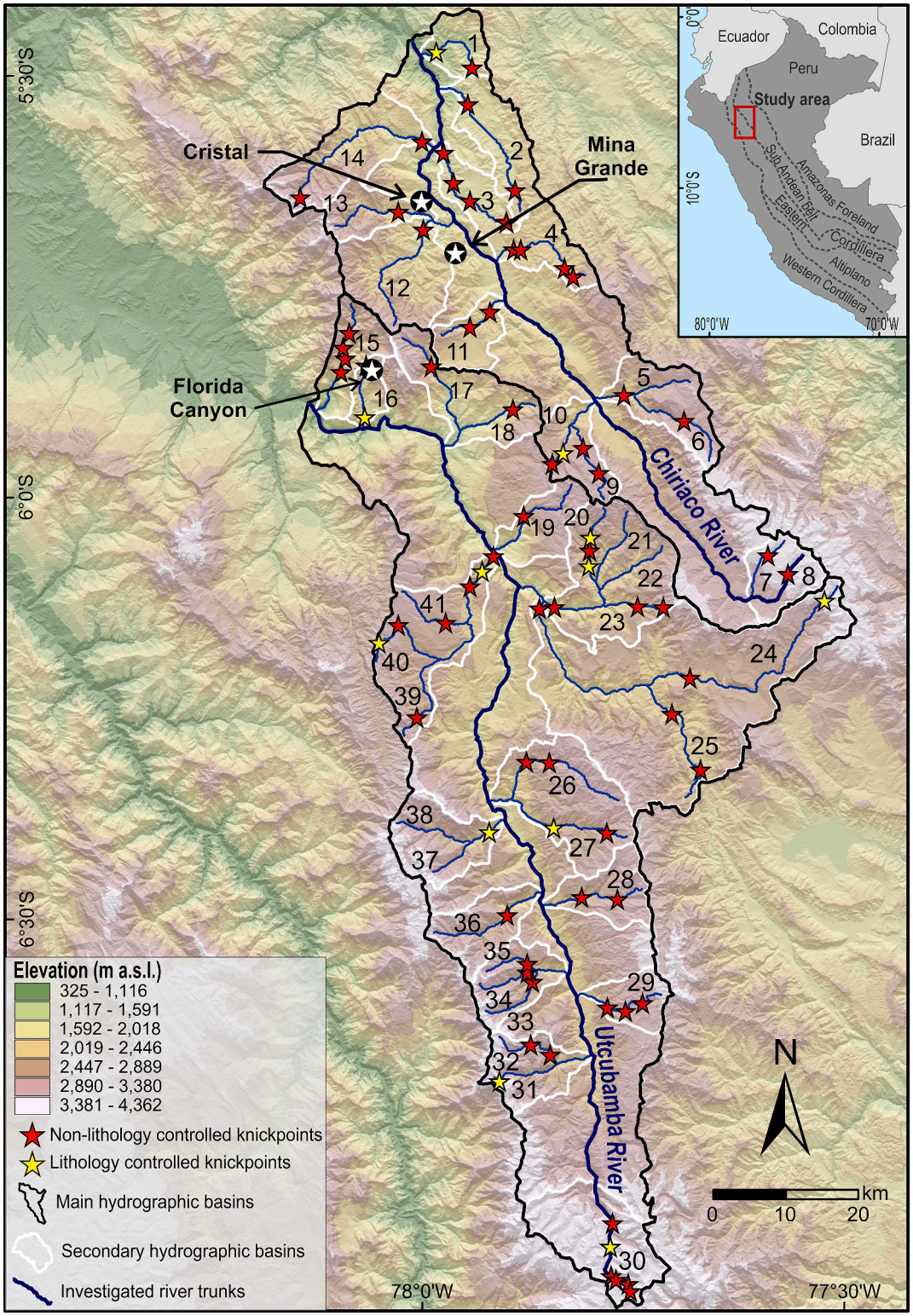


Fig. 6. Location of the knickpoints plotted on the elevation map of the Utcubamba and Chiriaco River basins. The lithology-controlled knickpoints, yellow stars, are distinguished from non-lithology-controlled knickpoints, red stars. The main trunks and the tributaries (in blue), numbered from 1 to 41, and the corresponding hydrographic sub-basins (in white) are represented.

of the maximum, minimum and mean elevations, which converge towards the same altitude of a few hundred meters above sea level, and that is also associated with an abrupt decrease of the local relief.

The above described features are also synthesized in Table 1.

4.2. River network features

River long profiles and chi-plots analysis has been carried out for 14 rivers pertaining to the Chiriaco River basin and for 27 rivers of the Utcubamba River basin(Fig. 6).

Overall, investigated trunks have chi-plots that range in shape from

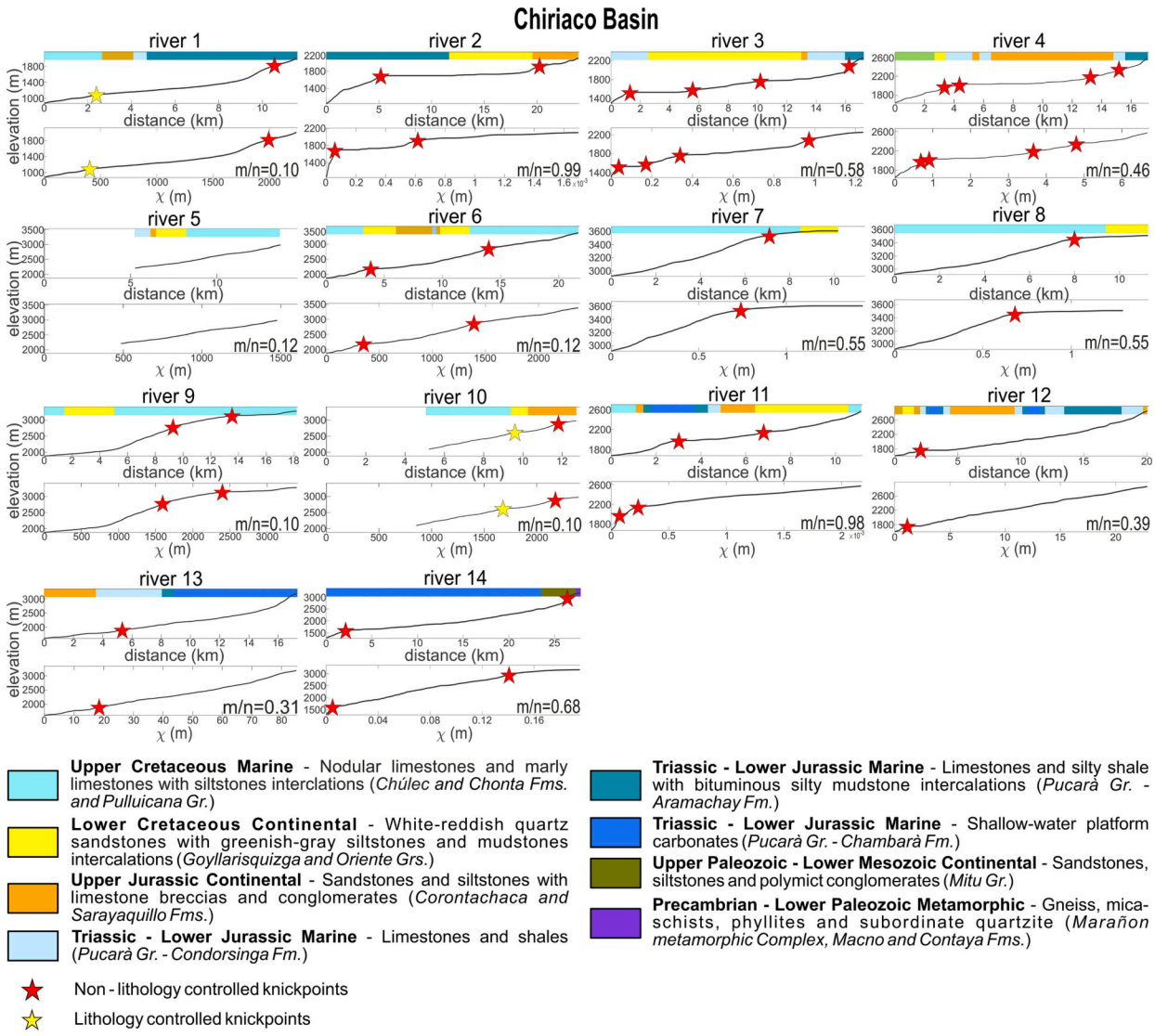


Fig. 7. Longitudinal profiles and transformed longitudinal profiles (chi plots) of 14 rivers that dissect the Chiriaco Basin (river numbering as in Fig. 6). Coloured bars indicate the lithology of the bedrock crossed by the river.

convex upward to slightly rectilinear with transient signals. We identified 76 knickpoints with variable amplitudes ranging from small steps of a few tens of meters to larger steps of hundred meters and to convex segments. The knickpoints are equally scattered along the left and right flanks of the two river basins (Fig. 5). Their position was compared with the lithology of the underlying bedrock and with the tectonic structures (Fig. 1) to assess the related control. The 76 recognized knickpoints were classified as either lithology or non-lithology controlled knickpoints, the latter of which are more abundant as they mainly occur in areas with homogeneous rock-types and are often placed in correspondence of major tectonic structures.

The Chiriaco River and its tributaries (Fig. 7) cross Cretaceous marine and continental units that outcrop to the SE and pass, towards the NW, to the Triassic rock of the Pucará Group. Chi-plots seem to be insensitive to lithology as convex upward chi-plots and transient signals occur both in the north-western and the south-eastern portions of the basin. Moreover, river long profiles and chi-plots suggest the occurrence of remnants of hanging low-relief surfaces marked by non-lithology controlled knickpoints. Such low relief surfaces, some of which are shown in Fig. 4, are carved by the Chiriaco River and its tributaries and occur at elevation around 1500 m (rivers n. 3), 1800 m (rivers n. 1, 2, 12, 14), 2000 m (rivers n. 2, 4, 11, 13), 2200 m (rivers n. 6, 11), 3000 m (rivers n. 6, 9, 10) and 3500 m (rivers n. 7, 8). In the Utcubamba River basin, tributaries in the right flank (rivers 15 to 30 in Fig. 8) mainly cross the rocks of the Pucará Group and the Mitu Group, and present on average convex chi plots with most knickpoints at elevation ranging from 1500 to 2500 m (Fig. 8), some of which are hundreds of meters high (i.e., rivers 15, 19 and 24 in Fig. 8). On the opposite, tributaries in the left flank flow through the basement crystalline rocks (rivers 31 to 38) and the Cretaceous limestones(rivers 39 to 41): the former have rectilinear chi-plot with few knickpoints whereas the latter have rectilinear to convex chi-plots with slight transient signals if compared with rivers flowing in the same rock-type but in the hydrographic right flank of the basin. Also in the Utcubamba River basin transient signal point the occurrence of remnants of hanging low relief surfaces (see also Fig. 4) marked by non-lithology controlled knickpoints. Such surfaces occur at elevations around 1500 m (river n. 15), 2000 m (river n. 15), 2100 m (river n. 25), 2500 m (rivers n. 17, 19, 20, 24, 33, 35, 41), 2700 m (rivers n. 26, 27, 28, 29, 40, 41), 3000 m and above (rivers n. 29, 30, 31, 32).

Noteworthy, comparison of low-relief surfaces within the two investigated basins suggest that transient signals in the Chiriaco River basin mark the occurrence of larger surfaces, with an horizontal extension up to 12–15 km (rivers n. 2 and 4 in Fig. 7), whereas low relief surfaces in the Utcubamba River basin consist of small remnants with

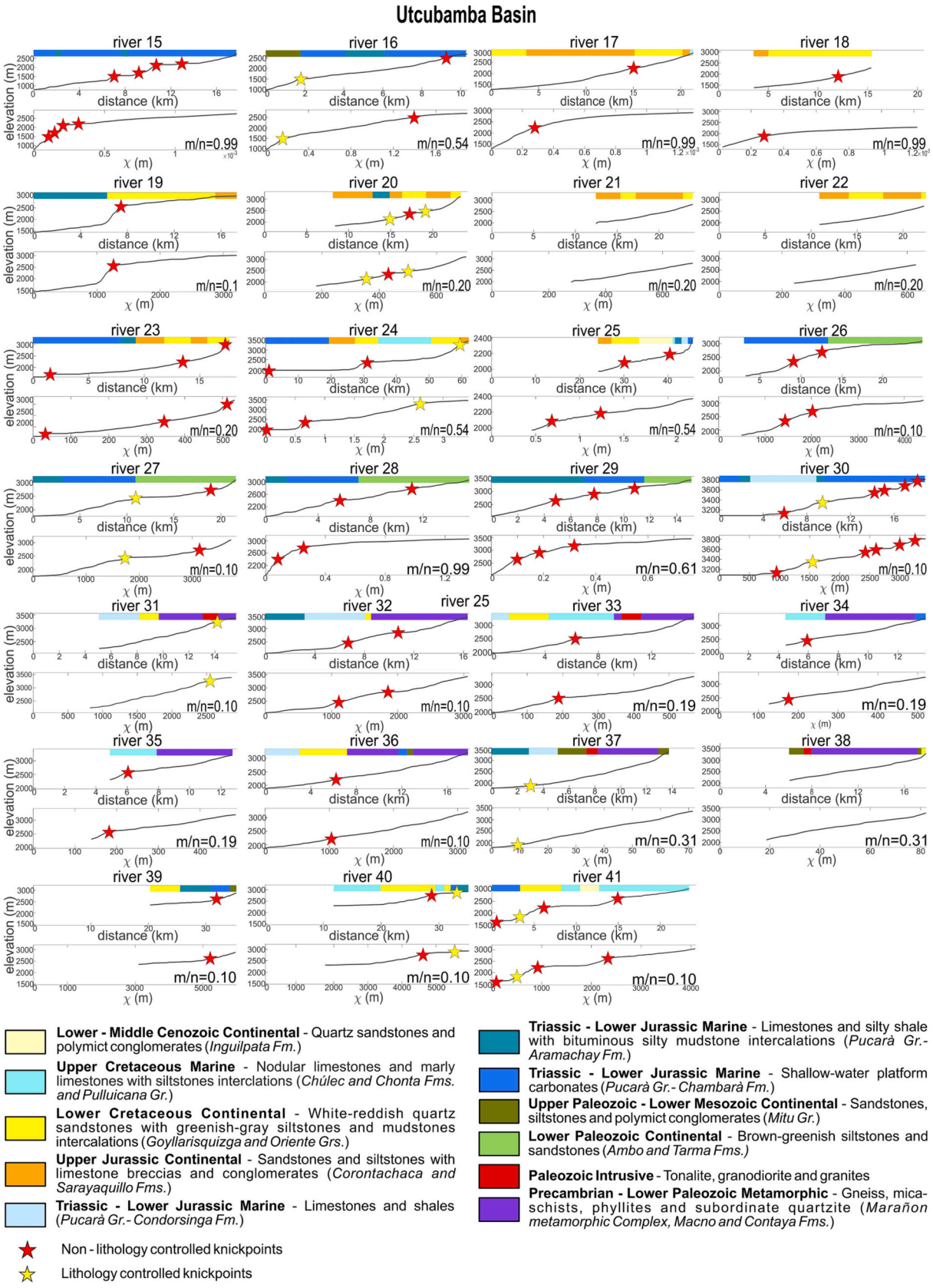


Fig. 8. Longitudinal profiles and transformed longitudinal profiles (chi plots) of the 27 rivers of the Utcubamba River Basin (river numbering as in Fig. 6). Coloured bars indicate the lithology of the bedrock crossed by the river.

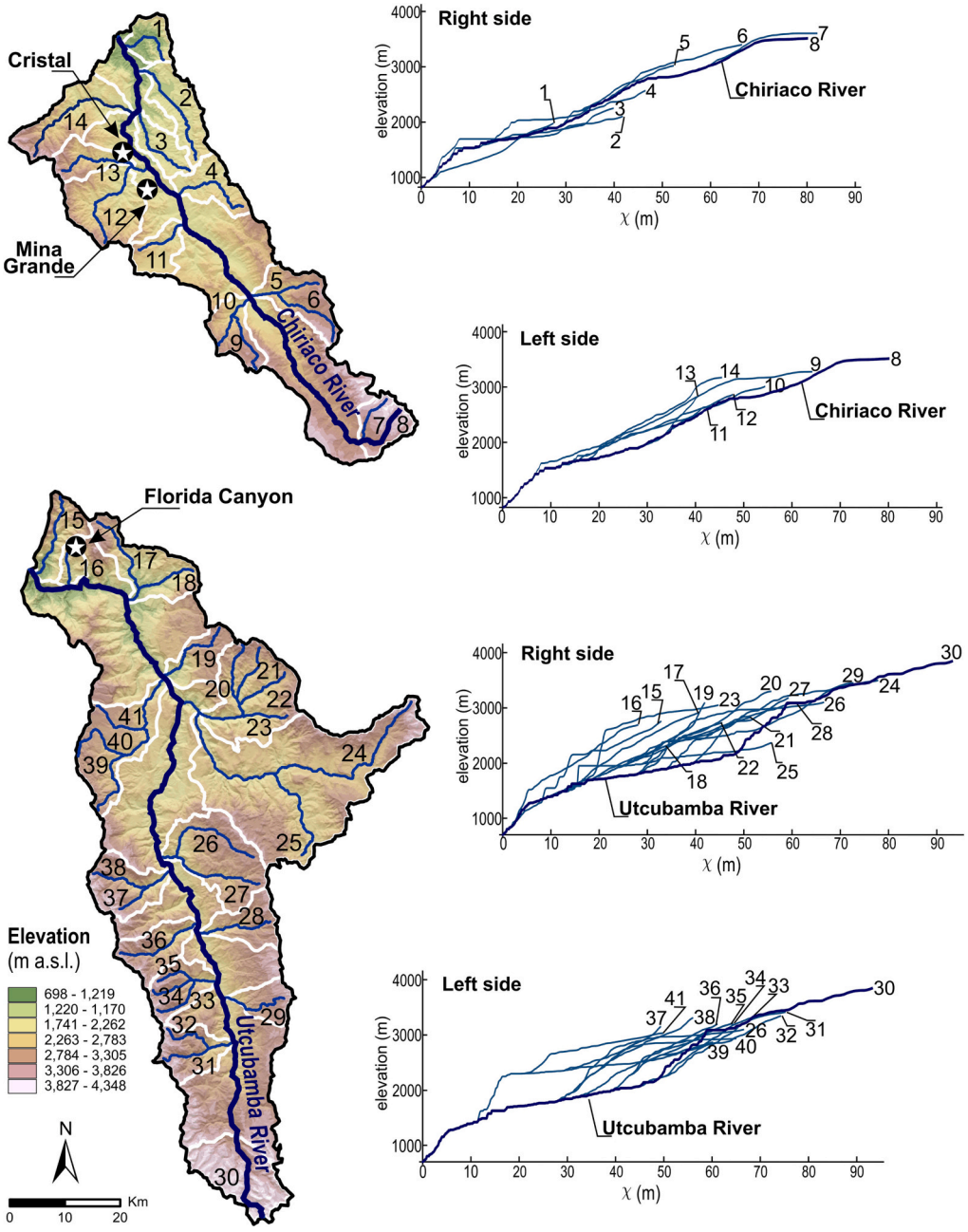


Fig. 9. Transformed longitudinal profiles of right and left bank rivers of the Chiriaco and Utcubamba River basins. The chi plots were constructed using a smoothing window of 250 m, a reference drainage area $A_0 = 1$ km^2 and a mean value of θ equal to 0.37.

limited horizontal extension, that just in one case (river n. 24 of Fig. 8) is comparable to those in the Chiriaco River basin. Overall data suggest that rivers in the south-western sector of the Utcubamba River basin are close to steady-state condition whereas transient signals not related to variable rock-types became abundant to the north, i.e. in the right flank of the Utcubamba River basin and in the Chiriaco River basin.

To further investigate river network features, we have compared chi-plots of all investigated rivers using the m/n value derived by averaging best fit values of each investigated trunk. The resulting θ_{ref} is 0.37 (Fig. 9). Again, rivers in right banks of the Utcubamba River basin and in left banks of the Chiriaco River basin are characterized by irregular chi plots with overall convex trends, interrupted, in some cases, by large knickpoints (e.g., rivers 10, 15, 19, 25, 30). On the opposite, rivers in left banks of the Utcubamba exhibit less pronounced knickpoints and some rectilinear chi plots (e.g., rivers 33, 34 and 36). Such an analysis points to the diffuse presence of transient signals in the investigated drainage basins but chi-plots in the Chiriaco River basin are steeper than chi-plots in the Utcubamba River basin. Considering that the lithological control on the origin of these transient signals has been excluded, such a difference may be interpreted as the result of differential rock uplift between the two basins, with an increasing trend of uplift towards the NE (i.e., towards the Chiriaco River basin).

To verify the uneven distribution of rock uplift, we have explored the spatial distribution of the k_{sn} index (Fig. 10). As k_{sn} index is mainly referred to bedrock rivers (Kirby and Whipple, 2012; Wobus et al., 2006), alluvial reaches included in Fig. 10 (i.e., the Utcubamba River and the Chiriaco River) have not been considered for interpretation. As a result, high k_{sn} values occur within the Chiriaco River basin (yellowish to reddish tones in Fig. 10) whereas k_{sn} index within the Utcubamba River exhibits low to very low values (bluish tones in Fig. 10).

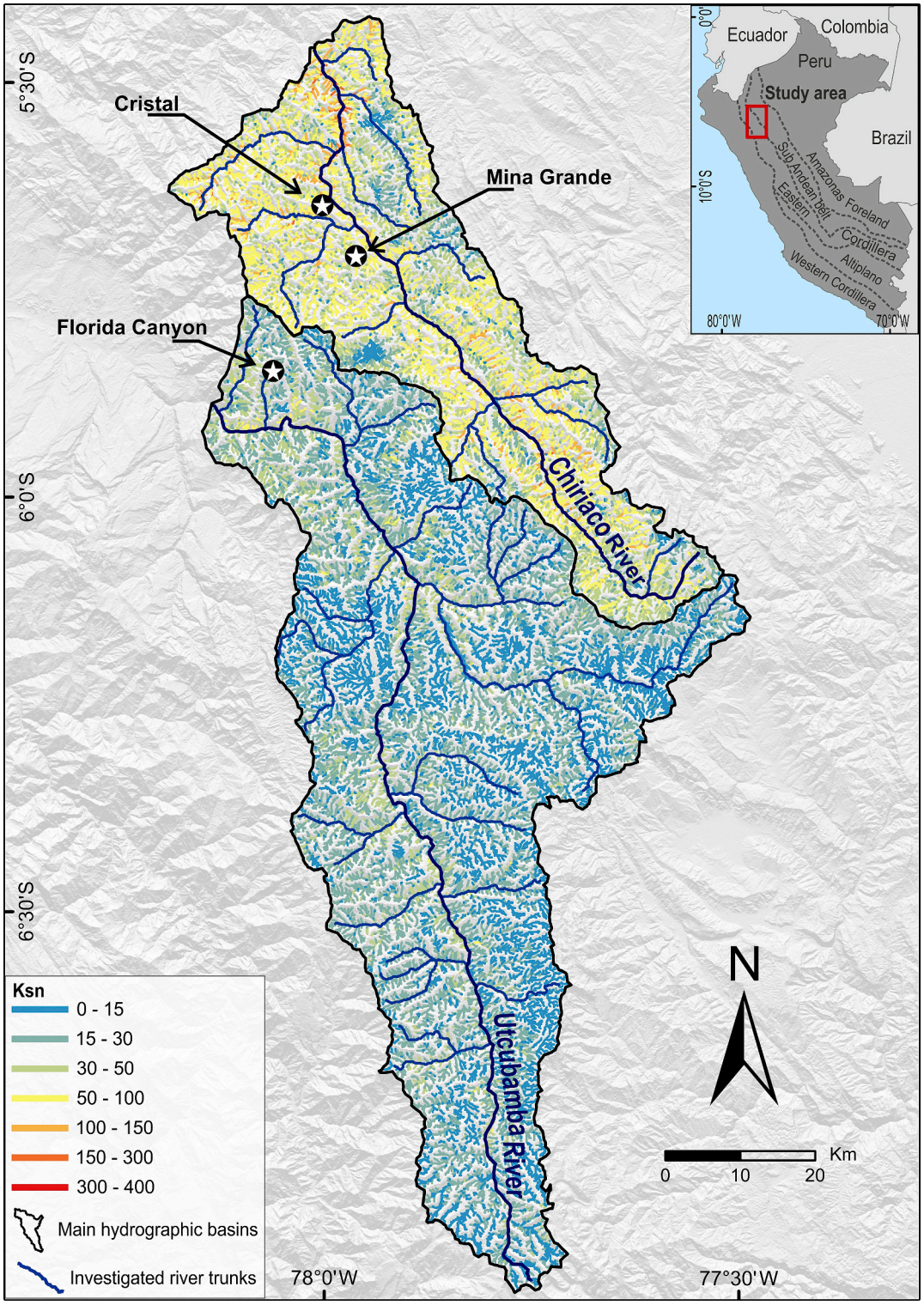


Fig. 10. Spatial distribution of the k_{sn} index along the Chiriaco and Utcubamba River basins. The k_{sn} map was constructed using the mean θ value = 0.37.

4.3. Detail scale analysis of the Bongará district

To further characterize the recognized NE oriented increasing trend in rock uplift, the topography and river network features were also studied along a detailed scale swath profile that runs in the northern sectors of the Utcubamba River and the Chiriaco River basins, thus crossing the three mineralized areas of Florida canyon, Mina Grande and Cristal. Furthermore, the swath crosses the low-erodibility Triassic rocks of the Pucará Group in the Utcubamba River basin and the high-erodibility Jurassic to Cretaceous units in the Chiriaco River basin. The same swath trace has been used to derive a curve showing the spatial distribution of the mean k_{sn} index (Fig. 11).

The Utcubamba River basin is characterized by maximum, mean and minimum elevations that increase towards NE at the boundary with the Chiriaco River basin, where the maximum elevation achieves 3500 m a.s.l. The dissecting Utcubamba River lowers the minimum elevations and

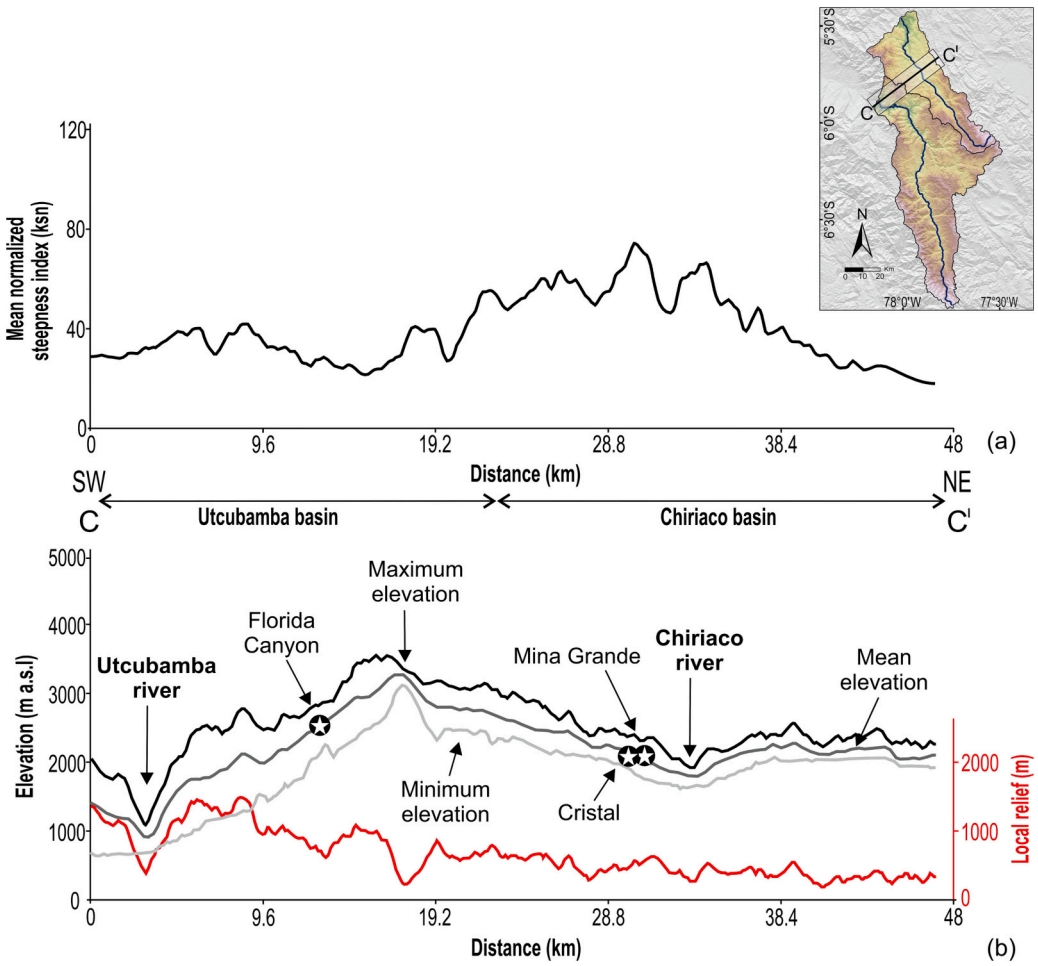


Fig. 11. (a) Profile representing the trend of the mean normalized steepness index (k_{sn}) along the transect CC′, 48 km-long and 10 km-wide, crossing the three mineralized areas. (b) Detail of the swath profile in Fig. 4 that follows the same path.

isolates remnants of low-relief surfaces (Fig. 4a–d) thus determining high values in the local relief. In addition, the low values of the mean k_{sn} testifies the predominance of river incision over uplift. This is consistent with the hypothesis of a more mature landscape shaped over the time by drainage systems. On the other hand, in the Chiriaco River basin the maximum, mean and minimum elevations exhibit higher values and stabilize around values of about 2500 m a.s.l. with a consequent sharp decrease in the local relief, and the mean k_{sn} index shows its highest values.

5. Discussion

The combined analysis of the topography and the river network points to different features between the Eastern Cordillera and the SAFTB (i.e., between the Utcubamba River and the Chiriaco River drainage basins, which correspond with the Florida Canyon and Mina Grande-Cristal prospect areas, respectively). Such a difference is suggested by high mean and minimum elevation (Fig. 5), by steeper chi-plots with large transient signals (Fig. 9) and by high to very high k_{sn} values in the surroundings of Cristal and Mina Grande mining areas (Fig. 11). Moreover, detail scale swath profile of Fig. 11 points to differences between the Utcubamba River and the Chiriaco River basins, as the trend of the elevation and relief curves may be interpreted as the result of a recently uplifted landscape in the Chiriaco River basin where rivers downcutting is overwhelmed by rock uplift. This is also coupled with a jump in the Ksn values within the Chiriaco River basin. In addition, comparison of the spatial distribution of the k_{sn} index (Fig. 10) with rock type (Fig. 1) suggests that high vs low values in such an index is not correlated with spatial distribution of “hard” vs “soft” lithologies. This enforces the interpretation of variable river network features between the Utcubamba River and the Chiriaco River basins due to input different from lithology and reasonably correlatable with tectonics. Furthermore, considering that high Ksn area is spread at the Chiriaco River basin scale, we may envisage that Ksn values register the effect of regional scale deformation rather than activity of some of the fault segments mapped in Fig. 1.

Analysis of the river network suggests that transient signals are correlated with phases of enhanced river incision that dissect hanging low relief surfaces. River incision is reasonably associated with tectonics, as lithology seems to play a less relevant role in shaping the landscape. This is inferred by the abundance of non-lithology controlled knickpoints (Fig. 6), and by the distribution of the k_{sn} index (Fig. 10), whose higher values occur at the Chiriaco River basin scale thus affecting rock-types with different erodibility (e.g., the Cretaceous marine and continental deposits and the Triassic Pucará Group deposits). The size of these low-relief surfaces, which are larger within the SAFTB (i.e., in the Chiriaco River basin and in river n. 24 of the Utcubamba River basin) suggest that tectonics-driven river incision occurred earlier in the Eastern Cordillera (i.e., in the Utcubamba River basin) where just small remnants of low relief surfaces occur (Figs. 4, 7 and 8). On the opposite, the larger low-relief surfaces in the SAFTB suggest that tectonics-driven river incision is recently shaping the landscape and had not enough time to reduce such surfaces to small remnants. Excluding the control role of glacio-eustasy and climate, the above described

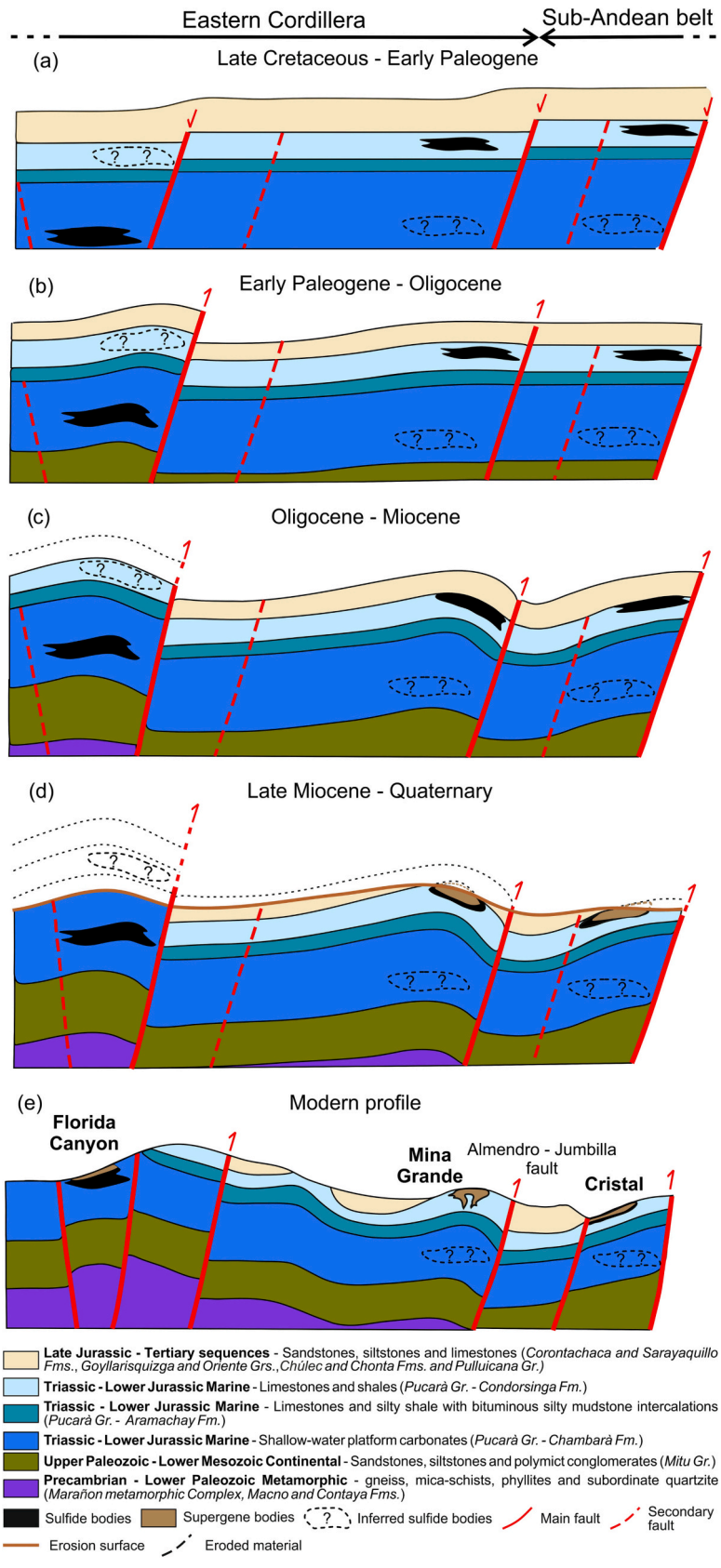


Fig. 12. Schematic model (not balanced) of the evolution of the rock uplift affecting the Eastern Cordillera and the SAFTB into the Bongará district, and related oxidation stages of pre-existing sulfides of Mina Grande and Cristal relatively to Florida Canyon. (a) Emplacement of the sulfide bodies during the Late Cretaceous-Early Tertiary in the same sedimentary basin at different depths: deeper for the Florida Canyon and shallower for Mina Grande and Cristal. (b) Since the Early Paleogene-Oligocene, the Andean deformation affected the Eastern Cordillera, firstly in its westernmost domain, in the Utcubamba River basin, causing the uplift of the Florida Canyon mineralization. (c) During the Oligocene- Miocene, deformation shifted to the East reaching the Cristal area, in the SAFTB. In the Florida Canyon site, the uplift was accompanied by the erosion of the upper levels of the succession. (d) During the Late Miocene, the sulfide bodies of Mina Grande and Cristal were brought to near-surface conditions earlier than the Florida Canyon one, resulting in the formation of supergene oxidized mineralization. (e) Modern situation showing the erosion of the entire Jurassic succession of the Pucará Group and of Tertiary sequences in correspondence of the Florida Canyon area, that brought the deposit to near-surface conditions.

features of topography and river network may be correlated with differential rock uplift between the Eastern Cordillera (i.e., the Utcubamba River basin) and the SAFTB (i.e., the Chiriaco River basin), with a NE oriented increasing trend.

These inferences are confirmed by the uplift data derived by thermochronological analysis conducted along transects across the orogen located a few hundred kilometres south with respect to our study area. In particular, from apatite fission track (AFT) analyses, (U—Th)/He (AHe) dating, and vitrinite reflectance (Ro) measurements, Eude et al. (2015) determined that the NE-verging propagation of the thrust wedge started first to the east of the Eastern Cordillera (between 30 and 24 Ma), and then in the SAFTB (between 24 and 17 Ma). In the Eastern Cordillera, the major shortening occurred between 24 and 17 Ma, whereas in the SAFTB shortening was mostly accommodated by thrusts between 17 and 8 Ma. Further shortening occurred in the last 8 Ma. The authors also suggested that rock exhumation was produced by erosion in response to thrust-related uplift (Eude et al., 2015). This clearly confirms that the Eastern Cordillera was affected by rock uplift and erosion earlier than the SAFTB, in agreement with the results of our morphometric analysis. The maximum time-averaged exhumation rate from the Late Cretaceous to the mid–late Miocene was estimated at ~0.08 mm/yr or less (Michalak et al., 2016).

The interpretation of the morphometric study finds indirect evidence in the altitude at which outcrop the rocks hosting the mineralization of the Florida Canyon, Mina Grande and Cristal and the observed alteration grade affecting the deposits.

In the district, the primary MVT sulfide mineralization formed inside the carbonate sequences of the Pucará Group deposited in a sedimentary basin around 74–84 Ma (during the Campanian period) in relation to burial and regional tectonics (Basuki et al., 2008; de Oliveira et al., 2020) that have driven the migration of the hydrothermal brine through the sedimentary basin towards and upward along steeply dipping normal faults (Fig. 12a). At Florida Canyon the mineralization is hosted within the Upper Triassic dolostone of the Chambará Formation (de Oliveira et al., 2020). The burial diagenesis of the carbonates of the Chambará Formation took place at 2500–3000 m below sea level (de Oliveira et al., 2020). At Mina Grande and Cristal, the mineralization is hosted in the Lower-Middle Jurassic limestone of the Condorsinga Formation, which is stratigraphically located at ~1000 m above the Chambará Formation hosting the Florida Canyon sulfides (Fig. 12a; Arfè et al., 2018; de Oliveira et al., 2020). Since the MVT sulfide mineralization formed at roughly the same time, at two different depths and currently outcrop at altitude, respectively, of ~2500 m a.s.l. for the Florida Canyon and of ~2000–2500 m a.s.l. for Mina Grande and Cristal, it implies that they must have undergone a differential rock uplift in terms of rates and time. In fact, the Utcubamba Basin, located in the Eastern Cordillera, was subjected to a first phase of uplift (Eude et al., 2015) that protracted in time and that, at some stage, was paired and overwhelmed by river downcutting, which resulted in low mean normalized steepness index. This would have allowed the slow erosion of the entire Jurassic succession (Fig. 12c–d) and the exposure at the surface of the Triassic-hosted mineralization (Fig. 12e). Otherwise, the Chiriaco Basin has experienced more recent rock uplift (Eude et al., 2015), which results in high minimum elevations and high mean k_{sn} values, low local relief and irregular long river profiles and chi plots with the presence of knickpoints (Fig. 12b–e). The more recent uplift of the SAFTB has exposed to weathering only the Jurassic-hosted Mina Grande-Cristal sulfide deposits resulting in the development of the supergene oxidized mineralization (Fig. 12e). If the Florida Canyon and the Mina Grande-Cristal deposits had been equally uplifted, the Zn mineralization of Mina Grande and Cristal would have been completely eroded and the economic deposits would not have formed. At the same time, it must be said that possible concealed Triassic-hosted sulfide deposits could be still located more in depth in the sedimentary succession below the Mina Grande- Cristal area (Fig. 12e).

6. Conclusion

The results of our morphometric study, applied to the Bongará district, provide new general insights on the processes that relate the genesis of supergene deposits to the vertical movements (e.g., rock uplift), in tectonically active areas. The coupling of uplift and river dissection promoted the unroofing and the exhumation of the sulfide mineralization, at different times and with different rates, which influenced the formation of the supergene deposits in the Florida Canyon and Mina Grande-Cristal areas.

The combined analysis of the topographic and river network features of the two hydrographic basins of Utcubamba and Chiriaco, allowed us to distinguish different portions of the belt with variable uplift. The Utcubamba River basin in the Eastern Cordillera is characterized by rugged local relief, low minimum elevations and low mean normalized steepness index. It is a mature landscape that has been shaped over time by river incision. This area experienced a long-lasting major uplift: this would have allowed slow erosion of the Jurassic succession and exposed on the surface the mineralization hosted in the Triassic succession, limiting the supergene alteration in the Florida Canyon. Otherwise, the Chiriaco Basin in the SAFTB is characterized by low local relief, high minimum elevations and high mean k_{sn} values with the presence of knickpoints. The SAFTB experienced more recent rock uplift and consequently minor erosion, which enabled the mineralization hosted in the Jurassic succession at Mina Grande-Cristal deposits. This scenario is consistent with the altitude at which the rocks hosting the mineralization of the Florida Canyon, Mina Grande and Cristal outcrop and justify the different mineralization styles of the three mineral deposits.

The morphometric analysis being a quite effective method in determining the landscape evolution in tectonically active areas, can be useful in distinguishing mountain ranges affected by different uplift and can be applied to all potentially ore deposit-fertile areas worldwide with near-surface ore bodies.

Declaration of competing interest

The authors declare that they have no known competing financial interests or personal relationships that could have appeared to influence the work reported in this paper.

Data availability

Data will be made available on request.

Acknowledgments

This work is part of the M.Sc. thesis of A. Sorrentino at the University of Naples (Supervisors: N. Mondillo and E. Valente). The work was carried out in the frame of a MoU between the DiSTAR (Naples) and Nexa Resources (Peru), project coordinator: N. Mondillo. We are grateful to two anonymous reviewers whose comments helped us to improve the manuscript.

References

Allmendinger, R.W., Jordan, T.E., Kay, S.M., Isacks, B.L., 1997. The evolution of the Altiplano-Puna plateau of the Central Andes. Annu. Rev. Earth Planet. Sci. 25, 139–174. https://doi.org/10.1146/annurev.earth.25.1.139.

Arfè, G., Mondillo, N., Balassone, G., Boni, M., Cappelletti, P., Di Palma, T., 2017a. Identification of Zn-bearing micas and clays from the Cristal and Mina Grande zinc deposits (Bongará Province, Amazonas Region, Northern Peru). Minerals 7 (11), 214. https://doi.org/10.3390/min7110214.

Arfè, G., Mondillo, N., Boni, M., Balassone, G., Joachimski, M., Mormone, A., Di Palma, T., 2017b. The karst-hosted Mina Grande nonsulfide zinc deposit, Bongará district (Amazonas region, Peru). Econ. Geol. 112, 1089–1110. https://doi.org/10.5382/econgeo.2017.4503.

Arfè, G., Mondillo, N., Boni, M., Joachimski, M., Balassone, G., Mormone, A., Santoro, L., Medrano, E.C., 2018. The Cristal Zn prospect (Amazonas region, Northern Peru).

Part II: an example of supergene enrichments in tropical areas. Ore Geol. Rev. 95, 1076–1105. https://doi.org/10.1016/j.oregeorev.2017.11.022.
Atherton, M., Webb, S., 1989. Volcanic facies, structure, and geochemistry of the marginal basin rocks of central Peru. J. S. Am. Earth Sci. 2, 241–261. https://doi.org/10.1016/0895-9811(89)90032-1.
Basilici, M., Ascione, A., Megna, A., Santini, S., Tavani, S., Valente, E., Mazzoli, S., 2020. Active deformation and relief evolution in the western Lurestan region of the Zagros mountain belt: new insights from tectonic geomorphology analysis and finite element modeling. Tectonics 39, e2020TC006402. https://doi.org/10.1029/2020TC006402.
Basuki, N., Spooner, E., 2008. Fluid evolution and flow direction of MVT Zn-Pb related basinal brines, Bongará area, northern Peru: CL and fluid inclusion data [abs.]. In: Presented at the Proceedings of the Geological-Mineralogical Association of Canada-Society of Economic Geologists—Society for Geology Applied to Mineral Deposits Meeting, Quebec, QC, Canada, pp. 26–28. https://doi.org/10.2113/gsecongeo.103.4.783.
Basuki, N., Spooner, E., 2009. Post-early Cretaceous Mississippi Valley-type Zn-Pb mineralization in the Bongara area, Northern Peru: Fluid evolution and paleo flow from fluid inclusion evidence. Explor. Min. Geol. 18, 25–39. https://doi.org/10.2113/gsemg.18.1-4.25.
Basuki, N., Taylor, B., Spooner, E., 2008. Sulfur isotope evidence for thermochemical reduction of dissolved sulfate in Mississippi Valley-type zinc-lead mineralization, Bongara area, northern Peru. Econ. Geol. 103, 783–799. https://doi.org/10.2113/gsecongeo.103.4.783.
Benavides-Cáceres, V., 1999. Orogenic Evolution of the Peruvian Andes: The Andean Cycle. https://doi.org/10.5382/SP.07.03.
Benjamin, M.T., Johnson, N.M., Naeser, C.W., 1987. Recent rapid uplift in the Bolivian Andes: evidence from fission-track dating. Geology 15, 680–683. https://doi.org/10.1130/0091-7613(1987)15<680:RRUITB>2.0.CO;2.
Boni, M., Mondillo, N., 2015. The “Calamines” and the “others”: the great family of supergene nonsulfide zinc ores. Ore Geol. Rev. 67, 208–233. https://doi.org/10.1016/j.oregeorev.2014.10.025.
Bowman, I., 1906. The Andes of southern Peru, Geological reconnaissance along the 73 meridian. Am. Geogr. Soc. Spec. Publ. 1, 336.
Brophy, J., 2012. NI 43-101 Technical Report Rio Cristal Resources Corp, 104. Bongará Zinc Proj.
Buscher, J.T., Ascione, A., Valente, E., 2017. Decoding the role of tectonics, incision and lithology on drainage divide migration in the Mt. Alpi region, southern Apennines, Italy. Geomorphology 276, 37–50. https://doi.org/10.1016/j.geomorph.2016.10.003.
Capitanio, F., Faccenna, C., Zlotnik, S., Stegman, D., 2011. Subduction dynamics and the origin of Andean orogeny and the Bolivian orocline. Nature 480, 83–86. https://doi.org/10.1038/nature10596.
Carlotto Caillaux, V.S., Acosta Pereira, H., Mamani Huisa, M.I., Cerpa Cornejo, L.M., Rodríguez Mejía, R., Jaimes Salcedo, F., Navarro Colque, P.A., Cueva Tintaya, E., Chacaltana Budiel, C.A., 2010. Los dominios geotectónicos del territorio peruano. https://hdl.handle.net/20.500.12544/2884.
Chacaltana Budiel, C.A., Valdivia Vera, W., Peña Guimas, D.F., Rodríguez Mejía, R., 2011. Geología de los cuadrángulos de Aramango y Bagua Grande, Hojas 11-gy 12-g, escala 1: 50,000-[Boletín A 142]. https://hdl.handle.net/20.500.12544/104.
Chacaltana Budiel, C.A., Valdivia Vera, W., Peña Guimas, D.F., Chumpitaz Ramírez, M. A., Benites Cañote, A.L., 2022. Geología del cuadrángulo de Jumbilla (hojas 12h1, 12h2, 12h3, 12h4)-[Boletín L 45]. https://hdl.handle.net/20.500.12544/3886.
Chavez, W.X., 2000. Supergene oxidation of copper deposits: zoning and distribution of copper oxide minerals. In: SEG Discovery, pp. 1–21. https://doi.org/10.5382/SEGnews.2000-41.fea.
Chew, D.M., Schaltegger, U., Kosler, J., Whitehouse, M.J., Gutjahr, M., Spikings, R.A., Miskovic, A., 2007. U-Pb geochronologic evidence for the evolution of the Gondwanan margin of the north-central Andes. Geol. Soc. Am. Bull. 119, 697–711. https://doi.org/10.1130/B26080.1.
Chew, D.M., Magna, T., Kirkland, C.L., Mišković, A., Cardona, A., Spikings, R., Schaltegger, U., 2008. Detrital zircon fingerprint of the Proto-Andes: evidence for a Neoproterozoic active margin? Precambrian Res. 167, 186–200. https://doi.org/10.1016/j.precamres.2008.08.002.
Chirico, R., Mondillo, N., Boni, M., Joachimski, M.M., Ambrosino, M., Buret, Y., Mormone, A., Leigh, L.E.N.B., Flores, W.H., Balassone, G., 2022. Genesis of the Florida Canyon Nonsulfide Zn Ores (Northern Peru): new insights into the supergene mineralizing events of the Bongará District. Econ. Geol. 117 (6), 1339–1366. https://doi.org/10.5382/econgeo.4941.
Cobbing, E., 1985. The tectonic setting of the Peruvian Andes. In: Magmat. Plate Edge Peruvian Andes Glasg. UK Blackie, pp. 3–12.
Cobbing, E.J., Pitcher, W.S., Wilson, J.J., Baldock, W.P., McCourt, W., Snelling, N.J., 1981. The Geology of the Western Cordillera of Northern Peru, 5. Inst. of Geol. Sci. Mem., p. 143p
Cobbing, E.J., Sánchez Fernández, A.W., Martínez Valladares, W., Zárate Olazabal, H., 1996. Geología de los cuadrángulos de Huaraz, Recuay, La Unión, Chiquián y Yanahuanca. Hojas: 20-h, 20-i, 20-j, 21-i, 21-j–[Boletín A 76]. https://hdl.handle.net/20.500.12544/199.
Coltorti, M., Ollier, C.D., 1999. The significance of high planation surface in the Andes of Ecuador. Geol. Soc. Lond., Spec. Publ. 162, 239–253. https://doi.org/10.1144/GSL.SP.1999.162.01.19.
DiBiase, R.A., Whipple, K.X., Heimsath, A.M., Ouimet, W.B., 2010. Landscape form and millennial erosion rates in the San Gabriel Mountains, CA. Earth Planet. Sci. Lett. 289, 134–144. https://doi.org/10.1016/j.epsl.2009.10.036.
England, P., Molnar, P., 1990. Surface uplift, uplift of rocks, and exhumation of rocks. Geology 18, 1173–1177. https://doi.org/10.1130/0091-7613(1990)018<1173:SUUORA>2.3.CO;2.
Eude, A., Roddaz, M., Brichau, S., Brusset, S., Calderon, Y., Baby, P., Soula, J., 2015. Controls on timing of exhumation and deformation in the northern Peruvian eastern Andean wedge as inferred from low-temperature thermochronology and balanced cross section. Tectonics 34, 715–730. https://doi.org/10.1002/2014TC003641.
Flint, J.-J., 1974. Stream gradient as a function of order, magnitude, and discharge. Water Resour. Res. 10, 969–973. https://doi.org/10.1029/WR010i005p00969.
Fontbote, L., Gorzawski, H., 1990. Genesis of the Mississippi valley-type Zn-Pb deposit of San Vicente, central Peru; geologic and isotopic (Sr, O, C, S, Pb) evidence. Econ. Geol. 85, 1402–1437. https://doi.org/10.2113/gsecongeo.85.7.1402.
Gallen, S.F., Wegmann, K.W., 2017. River profile response to normal fault growth and linkage: an example from the Hellenic forearc of south-central Crete, Greece. Earth Surf. Dyn. 5, 161–186. https://doi.org/10.5194/esurf-5-161-2017.
Garver, J., Reiners, P., Walker, L.J., Ramage, J., Perry, S., 2005. Implications for timing of Andean uplift from thermal resetting of radiation-damaged zircon in the Cordillera Huayhuash, northern Peru. J. Geol. 113, 117–138. https://doi.org/10.1086/427664.
Garzione, C.N., Hoke, G.D., Libarkin, J.C., Withers, S., MacFadden, B., Eiler, J., Ghosh, P., Mulch, A., 2008. Rise of the Andes. Science 320, 1304–1307. https://doi.org/10.1126/science.1148615.
Gregory-Wodzicki, K.M., 2000. Uplift history of the Central and Northern Andes: a review. Geol. Soc. Am. Bull. 112, 1091–1105. https://doi.org/10.1130/0016-7606(2000)112<1091:UHOTCA>2.0.CO;2.
Hack, J.T., 1957. Studies of Longitudinal Stream Profiles in Virginia and Maryland, 294. US Government Printing Office, pp. 45–97. https://doi.org/10.3133/pp294B.
Hedenquist, J.W., Arribas, A., 2022. Exploration implications of multiple formation environments of advanced argillic minerals. Econ. Geol. 117, 609–643. https://doi.org/10.5382/econgeo.4880.
Hitzman, M.W., Reynolds, N.A., Sangster, D., Allen, C.R., Carman, C.E., 2003. Classification, genesis, and exploration guides for nonsulfide zinc deposits. Econ. Geol. 98, 685–714. https://doi.org/10.2113/gsecongeo.98.4.685.
Hoorn, C., Wesselingh, F.P., Ter Steege, H., Bermudez, M.A., Mora, A., Sevink, J., Sanmartín, I., Sanchez-Meseguer, A., Anderson, C.L., Figueiredo, J.P., Jaramillo, C., Riff, D., Negri, F.R., Hooghiemstra, H., Lundberg, J., Stadler, T., Särkinen, T., Antonelli, A., 2010. Amazonia through time: Andean uplift, climate change, landscape evolution, and biodiversity. Science 330, 927–931. https://doi.org/10.1126/science.1194585.
Howard, A.D., Dietrich, W.E., Seidl, M.A., 1994. Modeling fluvial erosion on regional to continental scales. J. Geophys. Res. Solid Earth 99, 13971–13986. https://doi.org/10.1029/94JB00744.
https://earthdata.nasa.gov/ (last access on 18 May 2022).
https://geocatmin.ingemmet.gob.pe/geocatmin/ (last access on 1 September 2022).
Hunt, W., Pennington, J., S, D.H., PD, Osborn, J., Gilbertson, J., Tinucci, J., 2017. NI 43-101 Technical Report Preliminary Economic Assessment Florida Canyon Zinc Project Amazonas Department, Peru. SRK Consulting, US.
Isacks, B.L., 1988. Uplift of the central Andean plateau and bending of the Bolivian orocline. J. Geophys. Res. Solid Earth 93, 3211–3231. https://doi.org/10.1029/JB093iB04p03211.
Kirby, E., Whipple, K.X., 2001. Quantifying differential rock-uplift rates via stream profile analysis. Geology 29, 415–418. https://doi.org/10.1130/0091-7613(2001)029<0415:QDRURV>2.0.CO;2.
Kirby, E., Whipple, K.X., 2012. Expression of active tectonics in erosional landscapes. J. Struct. Geol. 44, 54–75. https://doi.org/10.1016/j.jsg.2012.07.009.
Laubacher, G., Naeser, C., 1994. Fission-track dating of granitic rocks from the Eastern Cordillera of Peru: evidence for Late Jurassic and Cenozoic cooling. J. Geol. Soc. 151, 473–483. https://doi.org/10.1144/gsjgs.151.3.0473.
Leach, D.L., Sangster, D.F., Kelley, K.D., Large, R.R., Garven, G., Allen, C.R., Gutzmer, J., Walters, S., 2005. Sediment-hosted Lead-Zinc Deposits: A Global Perspective, 105, pp. 593–625. https://doi.org/10.5382/AV100.18.
Mathalone, J.M., 1995. Petroleum geology of the sub-Andean basins of Peru. In: AAPG Special Volumes, pp. 423–444.
Mégard, F., 1978. Etude Geoloqique des Andes de Perou Central: Office de la recherche scientifique et technique outre-mer. (ORSTOM) Mem. 86, 310.
Mégard, F., 1984. The Andean orogenic period and its major structures in central and northern Peru. J. Geol. Soc. 141, 893–900. https://doi.org/10.1144/gsjgs.141.5.0893.
Mégard, F., 1987. Structure and evolution of the Peruvian Andes. In: Anat. Mt. Ranges, pp. 179–210. https://doi.org/10.1515/9781400858644.179.
Michalak, M.J., Hall, S.R., Farber, D.L., Audin, L., Hourigan, J.K., 2016. (U-Th)/He thermochronology records late Miocene accelerated cooling in the north-central Peruvian Andes. Lithosphere 8, 103–115. https://doi.org/10.1130/L485.1.
Molin, P., Pazzaglia, F.J., Dramis, F., 2004. Geomorphic expression of active tectonics in a rapidly-deforming forearc, Sila massif, Calabria, southern Italy. Am. J. Sci. 304, 559–589. https://doi.org/10.2475/ajs.304.7.559.
Mondillo, N., Arfè, G., Boni, M., Balassone, G., Boyce, A., Joachimski, M., Kang, J., Villa, I.M., 2018a. The Cristal Zinc prospect (Amazonas region, northern Peru). Part I: New insights on the sulfide mineralization in the Bongará province. Ore Geol. Rev. 94, 261–276. https://doi.org/10.1016/j.oregeorev.2018.01.021.
Mondillo, N., Arfè, G., Herrington, R., Boni, M., Wilkinson, C., Mormone, A., 2018b. Germanium enrichment in supergene settings: evidence from the Cristal nonsulfide Zn prospect, Bongará district, northern Peru. Mineral. Deposita 53, 155–169. https://doi.org/10.1007/s00126-017-0781-1.
Myers, J.S., 1976. Erosion surfaces and ignimbrite eruption, measures of Andean uplift in northern Peru Geol. J. 11, 29–44. https://doi.org/10.1002/gj.3350110104.

Myers, J.S., 1980. GEOLOGIA DE LOS CUADRANGULOS DE HUARMEY Y HUAYLLAPAMPA. HOJAS: 21-GY 21-H.
de Oliveira, S.B., Juliani, C., Monteiro, L.V.S., 2019a. Mineral characterisation of the non-sulphide Zn mineralisation of the Florida Canyon deposit, Bongará District, Northern Peru. Appl. Earth Sci. 128, 27–36. https://doi.org/10.1080/25726838.2018.1556033.
de Oliveira, S.B., Leach, D.L., Juliani, C., Monteiro, L.V., Johnson, C.A., 2019b. The Zn-Pb mineralization of Florida canyon, an evaporite-related Mississippi valley-type deposit in the Bongará district, northern Peru. Econ. Geol. 114, 1621–1647. https://doi.org/10.5382/econgeo.4690.
de Oliveira, S.B., Juliani, C., Monteiro, L.V., Tassinari, C.C., 2020. Structural control and timing of evaporite-related Mississippi Valley-type Zn–Pb deposits in Pucará Group, northern central Peru. J. S. Am. Earth Sci. 103, 102736 https://doi.org/10.1016/j.jsames.2020.102736.
de Oliveira, S.B., Johnson, C.A., Juliani, C., Monteiro, L.V., Leach, D.L., Caran, M.G., 2021. Geology and genesis of the Shalipayco evaporite-related Mississippi Valley-type Zn–Pb deposit, Central Peru: 3D geological modeling and C–O–S–Sr isotope constraints. Mineral. Deposita 56, 1543–1562. https://doi.org/10.1007/s00126-020-01029-w.
Olivetti, V., Cyr, A.J., Molin, P., Faccenna, C., Granger, D.E., 2012. Uplift history of the Sila Massif, southern Italy, deciphered from cosmogenic 10Be erosion rates and river longitudinal profile analysis. Tectonics 31, TC3007. https://doi.org/10.1029/2011TC003037.
Pérez-Peña, J.V., Al-Awabdeh, M., Azañón, J.M., Galve, J.P., Booth-Rea, G., Notti, D., 2017. SwathProfiler and NProfiler: two new ArcGIS Add-ins for the automatic extraction of swath and normalized river profiles. Comput. Geosci. 104, 135–150. https://doi.org/10.1016/j.cageo.2016.08.008.
Perron, J.T., Royden, L., 2013. An integral approach to bedrock river profile analysis. Earth Surf. Process. Landf. 38, 570–576. https://doi.org/10.1002/esp.3302.
Peruana, A., 2005. A Re–evaluation of the Geology and Mineralization of the Charlotte Bongará Zinc Project, Amazonas. Northern Peru: Technical Report.
Pfiffner, O.A., Gonzalez, L., 2013. Mesozoic–Cenozoic evolution of the western margin of South America: case study of the Peruvian Andes. Geosciences 3, 262–310. https://doi.org/10.3390/geosciences3020262.
Reid, C.J., 2001. Stratigraphy and Mineralization of the Bongara MVT Zinc-Lead District, Northern Peru (PhD Thesis).
Robustelli, G., 2019. Geomorphic constraints on uplift history in the Aspromonte Massif, southern Italy. Geomorphology 327, 319–337. https://doi.org/10.1016/j.geomorph.2018.11.011.
Rosas, S., Fontboté, L., Tankard, A., 2007. Tectonic evolution and paleogeography of the Mesozoic Pucará Basin, central Peru. J. S. Am. Earth Sci. 24, 1–24. https://doi.org/10.1016/j.jsames.2007.03.002.
Sánchez Fernández, A.W., 1995. Geología de los cuadrángulos de Bagua Grande, Jumbilla, Lonya Grande, Chachapoyas, Rioja, Leimebamba y Bolivar. Hojas: 12-g, 12-h, 13-g, 13-h, 13-i, 14-hy 15-h–[Boletín A 56]. https://hdl.handle.net/20.500.12544/177.
Schoenbohm, L.M., Whipple, K.X., Burchfiel, B.C., Chen, L., 2004. Geomorphic constraints on surface uplift, exhumation, and plateau growth in the Red River region, Yunnan Province, China. GSA Bull. 116 (7–8), 895–909. https://doi.org/10.1130/B25364.1.
Schwanghart, W., Kuhn, N.J., 2010. TopoToolbox: a set of Matlab functions for topographic analysis. Environ. Model. Softw. 25, 770–781. https://doi.org/10.1016/j.envsoft.2009.12.002.
Schwanghart, W., Scherler, D., 2014. TopoToolbox 2–MATLAB-based software for topographic analysis and modeling in Earth surface sciences. Earth Surf. Dyn. 2, 1–7. https://doi.org/10.5194/esurf-2-1-2014.
Sempere, T., Hérail, G., Oller, J., Bonhomme, M.G., 1990. Late Oligocene-early Miocene major tectonic crisis and related basins in Bolivia. Geology 18, 946–949. https://doi.org/10.1130/0091-7613(1990)018<0946:LOEMMT>2.3.CO;2.
Sillitoe, R.H., 2005. Supergene Oxidized and Enriched Porphyry Copper and Related Deposits. https://doi.org/10.5382/AV100.22.
Sillitoe, R.H., 2010. Porphyry copper systems. Econ. Geol. 105, 3–41. https://doi.org/10.2113/gsecongeo.105.1.3.
Sillitoe, R.H., McKee, E.H., 1996. Age of supergene oxidation and enrichment in the Chilean porphyry copper province. Econ. Geol. 91, 164–179. https://doi.org/10.2113/gsecongeo.91.1.164.
Sillitoe, R.H., Perelló, J., 2005. Andean Copper Province: Tectonomagmatic Settings, Deposit Types, Metallogeny, Exploration, and Discovery. https://doi.org/10.5382/AV100.26.
Snyder, N.P., Whipple, K.X., Tucker, G.E., Merritts, D.J., 2000. Landscape response to tectonic forcing: Digital elevation model analysis of stream profiles in the Mendocino triple junction region, northern California. Geol. Soc. Am. Bull. 112, 1250–1263. https://doi.org/10.1130/0016-7606(2000)112<1250:LRTTFD>2.0.CO;2.
Spikings, R., Reitsma, M., Boekhout, F., Mišković, A., Ulianov, A., Chiaradia, M., Gerdes, A., Schaltegger, U., 2016. Characterisation of Triassic rifting in Peru and implications for the early disassembly of western Pangaea. Gondwana Res. 35, 124–143. https://doi.org/10.1016/j.gr.2016.02.008.
Telbisz, T., Kovács, G., Székely, B., Szabó, J., 2013. Topographic swath profile analysis: a generalization and sensitivity evaluation of a digital terrain analysis tool. Z. Für Geomorphol. 485–513. https://doi.org/10.1127/0372-8854/2013/0110.
Tosdal, R.M., Clark, A.H., Farrar, E., 1984. Cenozoic polyphase landscape and tectonic evolution of the Cordillera Occidental, southernmost Peru. Geol. Soc. Am. Bull. 95, 1318–1332. https://doi.org/10.1130/0016-7606(1984)95<1318:CPLATE>2.0.CO;2.
Valente, E., Buscher, J.T., Jourdan, F., Petrosino, P., Reddy, S.M., Tavani, S., Corradetti, A., Ascione, A., 2019. Constraining mountain front tectonic activity in extensional setting from geomorphology and Quaternary stratigraphy: a case study from the Matese ridge, southern Apennines. Quat. Sci. Rev. 219, 47–67. https://doi.org/10.1016/j.quascirev.2019.07.001.
Van Laningham, S., Meigs, A., Goldfinger, C., 2006. The effects of rock uplift and rock resistance on river morphology in a subduction zone forearc, Oregon, USA. Earth Surf. Process. Landf. J. Br. Geomorphol. Res. Group 31, 1257–1279. https://doi.org/10.1002/esp.1326.
Whipple, K.X., Tucker, G.E., 1999. Dynamics of the stream-power river incision model: Implications for height limits of mountain ranges, landscape response timescales, and research needs. J. Geophys. Res. Solid Earth 104, 17661–17674. https://doi.org/10.1029/1999JB900120.
Whipple, K.X., Hancock, G.S., Anderson, R.S., 2000. River incision into bedrock: Mechanics and relative efficacy of plucking, abrasion, and cavitation. Geol. Soc. Am. Bull. 112, 490–503. https://doi.org/10.1130/0016-7606(2000)112<490:RIIBMA>2.0.CO;2.
Wilson, J.J., Reyes, L., Garayer, J., 1967. Geologia de los cuadrangulos de Mollebamba, Tayamba, Huaylas, Pomabamba, Caruaz y Huari. https://hdl.handle.net/20.500.12544/133.
Wobus, C.W., Crosby, B.T., Whipple, K.X., 2006. Hanging valleys in fluvial systems: controls on occurrence and implications for landscape evolution. J. Geophys. Res. Earth Surf. 111 https://doi.org/10.1029/2005JF000406.
Workman, A., Breede, K., 2016. Technical Report on the Bongará Zinc Project in the Yambrasbamba Area, Northern Peru. NI 43-101 Technical Report.
Wright, C., 2010. Rio Cristal Resources Corporation Bongará Zinc Project. Tech. Rep. NI 43-101, p. 102.